

An integrated single cell and spatial transcriptomic map of human white adipose tissue

Received: 2 December 2022

Accepted: 27 February 2023

Published online: 15 March 2023

 Check for updates

Lucas Massier¹, Jutta Jalkanen¹, Merve Elmastas¹, Jiawei Zhong¹, Tongtong Wang², Pamela A. Nono Nankam³, Scott Frendo-Cumbo¹, Jesper Bäckdahl¹, Narmadha Subramanian¹, Takuya Sekine⁴, Alastair G. Kerr¹, Ben T. P. Tseng¹, Jurga Laucinkiene¹, Marcus Buggert⁴, Magda Lourda^{4,5}, Karolina Kublickiene⁶, Nayanika Bhalla⁷, Alma Andersson⁷, Armand Valsesia⁸, Arne Astrup⁹, Ellen E. Blaak¹⁰, Patrik L. Ståhl⁷, Nathalie Viguerie^{11,12}, Dominique Langin^{11,12,13,14}, Christian Wolfrum², Matthias Blüher^{3,15}, Mikael Rydén^{1,16}  & Niklas Mejhert^{1,16} 

To date, single-cell studies of human white adipose tissue (WAT) have been based on small cohort sizes and no cellular consensus nomenclature exists. Herein, we performed a comprehensive meta-analysis of publicly available and newly generated single-cell, single-nucleus, and spatial transcriptomic results from human subcutaneous, omental, and perivascular WAT. Our high-resolution map is built on data from ten studies and allowed us to robustly identify >60 subpopulations of adipocytes, fibroblast and adipogenic progenitors, vascular, and immune cells. Using these results, we deconvolved spatial and bulk transcriptomic data from nine additional cohorts to provide spatial and clinical dimensions to the map. This identified cell-cell interactions as well as relationships between specific cell subtypes and insulin resistance, dyslipidemia, adipocyte volume, and lipolysis upon long-term weight changes. Altogether, our meta-map provides a rich resource defining the cellular and microarchitectural landscape of human WAT and describes the associations between specific cell types and metabolic states.

White adipose tissue (WAT) is a uniquely plastic organ that can expand or shrink in response to caloric supply and demand. The ability to function across pronounced variations in tissue mass is governed by a plethora of resident and recruited cell types¹. Disturbed WAT remodeling leads to changes in the cell composition of the tissue, which in turn increases the risk of developing insulin resistance, type 2 diabetes, and other cardiometabolic complications². Defining the cellular landscape and microarchitecture of human WAT in health and disease is therefore of considerable clinical relevance.

To determine cell composition, single-cell technologies have been applied to WAT obtained from different depots. Together,

these studies have identified novel specialized cells in adipose tissue such as: (i) adipogenic precursor cells with anti-adipogenic effects^{3–5}, (ii) lipid-associated macrophages (LAMs) with central roles in metabolic health⁶ and (iii) adipocyte subtypes with distinct sensitivities to insulin⁷ or thermogenic effects⁸. However, a caveat with most single-cell studies is that issues related to data production restrict sequencing depths and the number of samples that can be processed. Consequently, most published reports in the adipose field are based on small cohort sizes and even the largest ones have, so far, included fewer than 15 individuals^{9,10}. This, together with qualitative differences between technical platforms and

bioinformatic approaches, limits the generalizability of the observed findings.

To address this, we performed a comprehensive meta-analysis of newly generated and publicly available data where we integrated single-cell (scSeq) and single-nucleus (snSeq) RNA sequencing results. Based on this, we created a cellular meta-map which we used to deconvolve spatial and bulk transcriptomic data from women and men spanning over a very broad range in age, BMI, and metabolic states. By mining this rich resource, we provide a nomenclature of cells residing in human WAT, their localization and how they relate to metabolic health.

Results

Human WAT contains four major cell classes

To define the cellular landscape of human WAT, we retrieved scSeq, snSeq and spatial transcriptomic (STx) results from ten published reports comprising samples from subcutaneous, visceral, and perivascular WAT^{6–15}. We combined this with unpublished data from four additional cohorts (Massier et al. #1–4), resulting in a total of 17 datasets across studies and depots (Supplementary Table 1). As displayed in Fig. 1a, together these included 401,320 quality-filtered cells/nuclei (hereafter referred to as objects) obtained from 103 samples of 83 donors spanning over a broad range in age (22–77 years) and body mass index (BMI, 17–55 kg/m²).

To create a meta-map, we first defined cell clusters by processing all datasets individually using *Seurat v4.1*¹⁶ (Supplementary Fig. 1a and Supplementary Data 1). Based on these results, we calculated a Jaccard index comparing cell cluster marker genes between studies. We found that all data, except the one from Hildreth et al.¹¹, largely overlapped (Fig. 1a). This demonstrates that: (i) most cell types were present across the different cohorts/depots and (ii) snSeq, scSeq, and STx on average capture similar trends. Because STx is a spot-based approach that requires specific tools for data deconvolution¹⁷, we analyzed the Bäckdahl et al.⁷ study separately. For the remaining snSeq/scSeq datasets, we performed a high-level topological analysis, which revealed that clusters identified in the individual studies separated into four major cell classes: adipocytes, fibroblast and adipogenic progenitors (FAPs), vascular and immune cells (Fig. 1b). To validate our findings, we applied *CellTypist*¹⁸ to the immune cells which confirmed our annotations for this class (Supplementary Fig. 1b).

Our comprehensive classification allowed us to estimate the cellular composition of WAT (Fig. 1c, d). For this, we first used snSeq data, as this method, in contrast to scSeq, captures fat cells. After quantifying the number of adipocytes in each dataset, we next compared the proportions of the other cell classes between methods. We found that FAPs constituted the largest class of ~40% of the total cell population according to both snSeq and scSeq. This was followed by adipocytes and immune cells, which were present in a 1:1 ratio and together constituted ~40% of the cells. For adipocytes, this is in line with what has previously been reported in the literature¹⁹. About 15% of the objects were vascular cells, but the recovery of this cell class was strongly influenced by methods where the proportion was approximately three times higher with snSeq compared to scSeq. This could be due to pre-selection bias introduced by enzymatic digestion as has been shown before for endothelial cells in mouse kidney²⁰. Comparisons across depots showed that there were no significant differences in cell class abundance. As expected, scSeq studies where cells had been enriched for either FAPs (CD45⁻)¹³ or immune cells (CD45⁺)¹⁴ prior to sequencing displayed markedly higher proportions of these cell types compared to the rest of the datasets, supporting the validity of our classification (Supplementary Fig. 1a). Of note, for perivascular WAT, snSeq data were only available from one cohort implying that the generalizability of the results from this depot needs to be further validated.

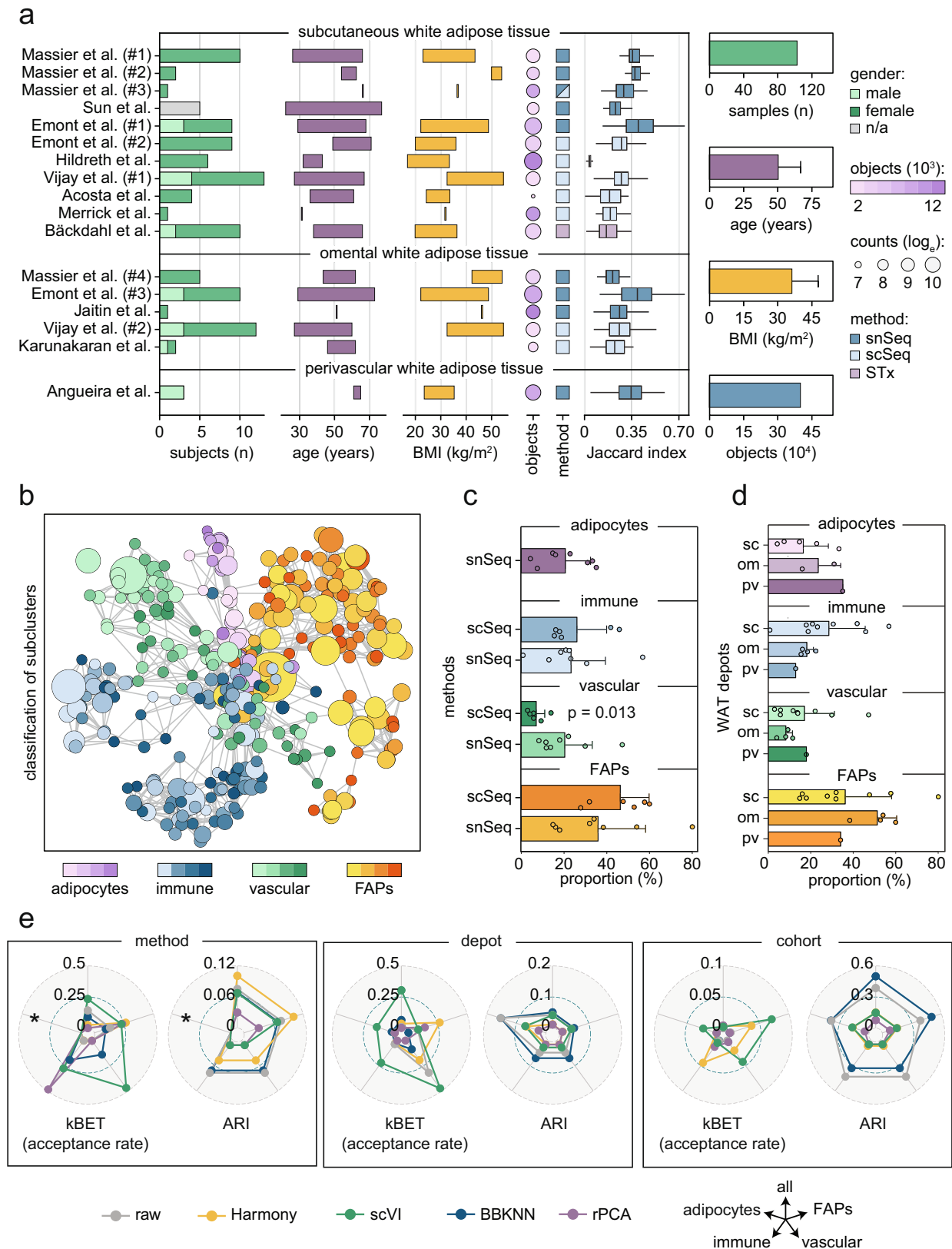
Cell class-based analyses successfully integrates data across studies

As much of the biological variability overlapped between cohorts, we performed data integration across studies. In contrast to the label-centric analysis presented in Fig. 1b, this approach facilitates the identification of rare cell types which risk being omitted in more sparsely sampled datasets. Many tools are available for integrative analyses and all of them introduce different biases where a trade-off between overfitting *vs.* insufficient integration must be considered^{21,22}. In a first step, we applied *single-cell annotation using variational inference (scANVI)* as prior knowledge of cell type annotations can improve integration results²³. In line with the findings in Fig. 1a, b, data from Hildreth et al. could not be integrated with *scANVI* and this dataset was therefore excluded from all subsequent analyses (Supplementary Fig. 1c). After removing Hildreth et al. the *scANVI* results mirrored the high-level topological analysis shown in Fig. 1b (Supplementary Fig. 1d). We therefore split the data into these four classes and tested different integrative frameworks. We included *reciprocal principal component analysis (rPCA)*¹⁶, *batch balanced k-nearest neighbors (BBKNN)*²⁴, *Harmony*²⁵ and *single-cell variational inference (scVI)*²⁶, as all of them have benchmarked well in prior systematic comparisons^{27,28}. To evaluate these methods across the main confounders (techniques, depots and cohorts), we calculated the adjusted Rand index (ARI)²⁹, k-nearest-neighbor batch-effect test (kBET)³⁰ and Local Inverse Simpson Index (LISI)^{25,31}. In comparison to using all objects as input, we obtained enhanced integration results when splitting the data into immune cells, vascular cells, FAPs, and adipocytes. Our results showed that (i) *Harmony* performed well for FAP integration, (ii) *scVI* and *rPCA* provided the best results across all scores for methods, cohorts, and depots, and (iii) kBET showed overall the lowest rejection rates for *scVI* (Fig. 1e, Supplementary Fig. 2a, b). This in combination with a previous report suggesting that *scVI* works best for complex data²⁷, prompted us to apply this method to all four cell classes separately. Given that the included datasets varied in object number, we capped them to contain similar object counts to reduce bias and enhance integration (Supplementary Fig. 2c, d). Based on this, we included an optimal number of objects for each cell class which resulted in cell clusters represented by most studies and methods (Supplementary Fig. 2d, e). With these criteria, we created WAT annotation models which are publicly available and can be applied in future studies (see Methods).

Immune cells with different origins and activation states are present in human WAT

The immune cell class integrated well across techniques, studies, and depots (Fig. 1e, Supplementary Fig. 2b). As displayed in Supplementary Figures 3a, b, we annotated two major groups containing distinct subpopulations of: (i) T, natural killer (NK), and NKT cells (28.8%) and (ii) monocytes, macrophages, and dendritic cells (67.3%) as well as three minor populations including mast (2.94%), B (0.87%), and plasma B cells (0.16%).

The large number of objects allowed us to further dissect these groups separately to provide a high-resolution map of the different cell populations. In the major lymphocyte group, we identified 11 different clusters which were denoted lyC0–10, in order of abundance from high to low (Fig. 2a, b, Supplementary Table 2 and Supplementary Data 2). These included subtypes of (i) Th1-polarized (lyC0), tissue-resident memory (T_{RM}, lyC01), naive/early differentiated (lyC04), and naive/regulatory (T_{REG}, lyC08) CD4⁺ T cells (ii) CD8⁺ T cells including early- (lyC02) and late-differentiated (lyC03) cells, (iii) NKT cells (lyC05), as well as (iv) CD16⁺ (lyC06) and CD16⁻ (lyC09) NK cells. Multiple cell classes, including T_{REG} and T_{RM}, could be further subdivided based on their differentiation states (Fig. 2a, lower panel). We confirmed these data by flow cytometry (Supplementary Fig. 3c) using a panel of antibodies identified in the transcriptomic analyses (see Methods). Comparisons across depots revealed that all identified T and NK cell



populations were present in subcutaneous, omental, and perivascular WAT albeit with slightly different proportions (Fig. 2b). For example, Th1 CD4⁺ T cells (lyC0) were more abundant in omental while late-differentiated CD8⁺ T cells (lyC03) enriched in subcutaneous WAT (Fig. 2b). These observations were confirmed by deconvolution of bulk transcriptomic data in two independent cohorts^{32,33} (Fig. 2c).

We next classified the myeloid group. This resulted in 16 different clusters (myC0-15) including macrophages, non-classical (myC05) and classical (myC14) monocytes, as well as class 2 dendritic cells (myC03) (Fig. 2d, Supplementary Table 2 and Supplementary Data 2). In-depth analyses of macrophages revealed several M2-like subpopulations (myC0-01, myC04, myC07-09, myC11-13) out of which two (myC08

Fig. 1 | A meta-map to define human WAT composition. **a** For each included cohort, number (*n*) and gender of subjects, age (years) and body mass index (BMI) ranges (min–max) as well as number of objects (cells/nuclei), method (single-nucleus Seq [snSeq], single-cell Seq [scSeq] or spatial transcriptomics [STx]) and Jaccard index are displayed. Massier et al. #1–4 refer to data generated for the present meta-analysis and gray bars (*n/a*) indicate that no information was obtained. Boxes for age and BMI represent a range (min–max), boxplots are presented as interquartile range plus median and Tukey whiskers. Summarizing statistics are displayed in the right panels as mean ± S.D. **b** Network displaying nodes (subclusters from each study) and edges (marker gene overlap). Data were distributed into four major classes and named based on prominent marker genes. Node sizes are reflecting cluster proportions. The displayed network does not

include results from Hildreth et al.¹¹, as data from this study overlapped poorly with the others. **c, d** Cell class proportions comparing **c**) methods (snSeq vs. scSeq) and **d** depots (subcutaneous [sc] WAT vs. omental [om] vs. perivascular [pv]). Note that adipocytes are only available by snSeq. Data are shown as mean ± S.D. Statistical differences were calculated by two-sided Mann–Whitney *U* test between sc (*n* = 10) and om (*n* = 4) WAT or scSeq (*n* = 6) and snSeq (*n* = 8). Because of fewer cases, no statistics were calculated for adipocytes and pvWAT. **e** K-nearest-neighbor batch-effect test (kBET) and adjusted Rand index (ARI) for raw or integrated data using the indicated methods displayed according to method, depot, and cohort. BBKNN batch balanced k-nearest neighbors, scVI single-cell variational inference, rPCA reciprocal principal component analysis. Source data are provided as a Source data file.

and –12) have not been previously reported in WAT (Fig. 2d, e). We also identified mixed M1/M2-like (myC06), lipid-associated (LAM, myC02), metabolic-regulated (MMe, myC10) and redox-regulatory metabolic (Mox, myC15) macrophages (Fig. 2d). Similar to lymphoid cells, our flow-cytometry-based follow-up studies confirmed the presence of several of the identified myeloid subpopulations in subcutaneous WAT (Supplementary Fig. 3d). Analyses over the three depots revealed that LAMs (myC02) were present in both subcutaneous and omental WAT but were virtually absent in the perivascular depot, while Mox (myC15) were only present in the subcutaneous region (Fig. 2f). The omental region was enriched for different types of M2-like cells (myC07–08 and myC12), observations which were confirmed by deconvolution of bulk transcriptomic data (Fig. 2g). In addition to these larger groups, we also analyzed B and mast cells (Supplementary Fig. 3e, f, Supplementary Data 2). B cells separated into activated (bc01, characterized by upregulation of genes related to regulation of T cell-mediated cytotoxicity) and non-activated states (bc0). While mast cells could not be clearly subdivided, there were trends in the data indicating that both MC_T (tryptase-positive) and MC_{TC} (positive for chymase and carboxypeptidase) cells were present.

WAT contains vascular cells with angio- and adipogenic expression profiles

For vascular cells, our data integrated well between techniques, studies, and depots (Fig. 1e, Supplementary Fig. 2b). We identified 12 distinct cell populations (vCO–11), which were broadly split into four major groups including several blood (vCO–03, vCO5, vCO8–11), and lymphatic (vCO6) endothelial cells as well as vascular smooth muscle cells (vCO7) and pericytes (vCO4) (Fig. 3a, Supplementary Table 2 and Supplementary Data 2). Based on nomenclatures from several scSeq atlases, blood endothelial cells were further classified into the classical capillary (vCO), venous (vCO1 and vC11), mixed capillary/venous (vCO3), and arterial (vCO2) subpopulations (Fig. 3b). Three subtypes (vCO8–10) separated from the major endothelial cell populations. Top marker genes for these revealed that vCO8 displayed a considerable overlap with the herein-identified myC08 (Jaccard index: 0.33), indicating that they may represent cells with similar function or intermediate cell states. Two of the shared marker genes were *TIMPI* and *ITLN1* which encode secreted proteins inhibiting neovascularization^{34,35}, suggesting that these cells may exert anti-angiogenic effects (Fig. 3c). vCO9 was enriched for genes previously described in “early endothelial progenitor cells” (e.g., *TYROBP*, *FCER1G*), a hematopoietic cell type that promotes angiogenesis via paracrine mechanisms (Fig. 3d)^{36,37}. Thus, human WAT may contain vascular cells that either stimulate or inhibit vascularization. One vascular subtype (vCO5) expressed multiple marker genes for committed preadipocytes (e.g., *CXCL14*, *APOD*, and *CFD*) and was the only vascular population that expressed *PDGFRA* (Fig. 3e). In mice, all peri-aortic adventitial fibroblasts are *PDGFRA*⁺ and give rise to perivascular adipocytes¹⁵. It is therefore possible that vCO5 represents an intermediate cell state between endothelial and adipocyte precursor cells. Admittedly, this notion needs further

functional studies. Comparisons between depots revealed that all cell types, including vCO5, were present in the three regions. However, lymphatic (vCO6) and *TIMPI*-expressing (vCO8) endothelial cells were enriched in omental and perivascular WAT (Fig. 3f), observations which were confirmed by deconvolution of bulk transcriptomic data (Fig. 3g).

Subcutaneous FAPs include subpopulations distinguished by degree of commitment

Although FAPs include fibroblasts and stem cells at different stages of commitment, an established nomenclature for this class is still lacking. This, in combination with their pronounced heterogeneity and depot-specific contribution to WAT expansion (at least in mice³⁸), prompted us to analyze this cell class depot-by-depot. The subcutaneous FAPs separated into 17 clusters (sfCO–16) distributed into four smaller (sfCO3, –11, –13, and –16) and one very large (86.5% of all FAP objects) group (Fig. 4a and Supplementary Data 2). The former included mesothelial-like cells (sfC11), CD74⁺ stromal cells (sfC13) reported to have antifibrotic properties³⁹, and late committed preadipocytes (sfC16). One cluster (sfCO3) enriched for cell adhesion molecules and was the only FAP that did not express *CD34*, *PDGFRA*, or *PDGFRB* (Fig. 4b).

In contrast to the smaller clusters, the larger group included multiple extracellular matrix- and *CD55/PI16*-expressing cells (Fig. 4a, c, Supplementary Fig. 4a). The latter marks a universal fibroblast population that can differentiate into more specialized cells⁴⁰, including adipocytes¹⁵. Therefore, we used them as a starting point in pseudo-time analyses which identified two distinct trajectories (routes 1–2) branching into opposite directions at the first step (Fig. 4d). To test if these trajectories were recapitulated during de novo adipocyte formation, we deconvolved bulk RNAseq data from human CD55⁺ cells undergoing adipogenesis in vitro⁴¹ (Fig. 4e, f). Our results show that the *CD55/PI16* gene cluster (sfCO2) was highly expressed prior to differentiation and was markedly downregulated upon adipogenic induction (Fig. 4g). This was followed by a transient upregulation of route 1-localized clusters (sfCO4–05 and sfCO7–08), which thus constitute transient cell states. Route 1 ended in sfCO, a cell population enriched for genes that were upregulated at late stages of differentiation (e.g., *APOD* and *CFD*) and most likely represent committed preadipocytes (Fig. 4a, d, g). In contrast to route 1, the cell populations in route 2 (sfCO1, sfCO6, sfCO9–10, sfC12, and sfC14–15) could not be detected during in vitro adipogenesis. These results were recapitulated in three additional cell models^{41–43} (Supplementary Fig. 4b), suggesting that under standard in vitro conditions, CD55⁺ adipocyte precursor cells cannot recapitulate the full FAP heterogeneity observed in subcutaneous WAT.

To improve our FAP annotations and determine inter-species similarities, we systematically compared our findings with scSeq data obtained from mouse inguinal WAT (which is frequently used as a proxy for human subcutaneous WAT)^{3,5,44}. We found that mouse early adipocyte progenitors (P1-1 and P1-2) overlapped with *CD55/PI16*-expressing adipocyte precursors (sfCO2), while more committed

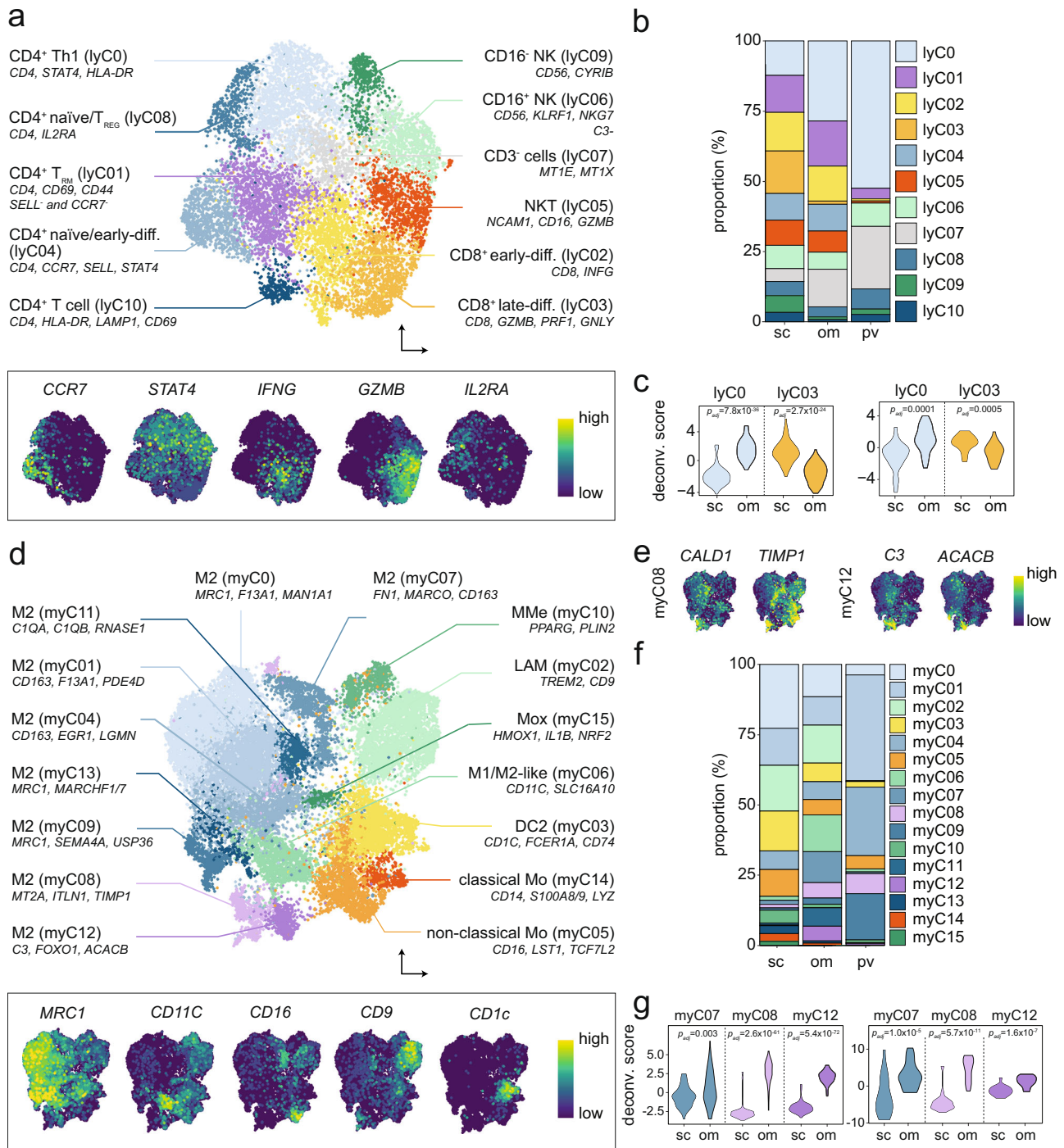


Fig. 2 | Analyses of the WAT immune cell panorama reveal novel subtypes. **a** Nomenclature (upper panel) and expression patterns of selected marker genes (lower panel) for T, NKT, and NK cells (lyC0-10). **b** Proportions (%) of T, NKT, and NK cells (lyC0-10) in subcutaneous (sc), omental (om), and perivascular (pv) WAT depots. **c** The enrichment of lyC0 in omental and lyC03 in subcutaneous WAT was supported by deconvolution of bulk transcriptomic data from Arner et al.³² (left panel) and Krieg et al.³³ (right panel). *p* values were calculated by two-sided Wilcoxon signed-rank test. **d** Same visualization as **a**, but for macrophages and

macrophages. **e** Selected marker gene expression profiles for omental-enriched myC08 and myC12. **f** Same visualizations as **b**, but for monocytes and macrophages. **g** Same as **c**, but for myC07, myC08, and myC12. DC dendritic cells, diff differentiated, LAM lipid-associated macrophages, MMe metabolic-regulated macrophages, Mo monocytes, Mox redox-regulatory metabolic macrophages, NK natural killer cells, NKT natural killer T cells, Th helper T cells, T_{REG} regulatory T cells, T_{RM} tissue-resident memory T cells. Source data are provided as a Source data file.

preadipocytes (P2-1 and P2-2) resembled sfC0 (Fig. 4h). The gene expression profile of the P3 population, which has been defined as FAPs with anti-adipogenic properties (A_{REG}), showed overlap with one of the transient cell clusters along route 1 (sfC04). There were no overlaps with any of the route 2-localized FAPs indicating that clusters along this trajectory are not overlapping with the Lin/SCA⁺ cells pre-

selected in the studies by Schwalie et al.³ and Dong et al.⁵. However, *DPP4*, which is an established marker of pro-adipogenic FAPs in mouse inguinal WAT⁴⁴, projected onto route 2 and was enriched in sfC06 and -10 (Supplementary Fig. 4c). This demonstrates that specific FAPs in this trajectory overlap with murine PDGFRB⁺ cells with adipogenic capacity.

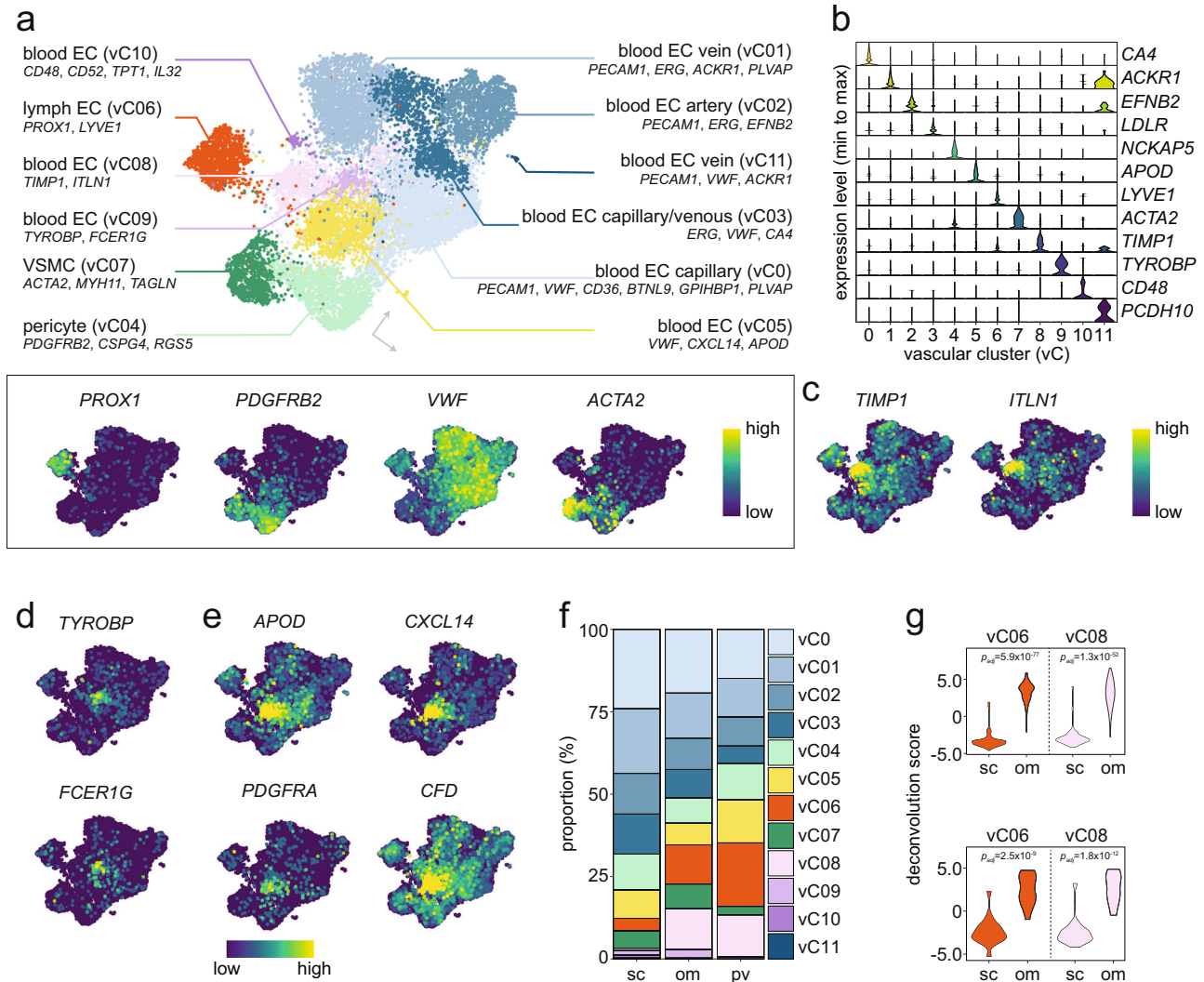


Fig. 3 | The vascular cell class contains mixed and intermediate cell states.
a, b Nomenclature and visualizations of selected marker genes for vascular cells (vC0-11), including **a** UMAPs and **b** violin plots. **c–e** Multiple UMAPs of marker genes for three subtypes of blood ECs (vC08, vC09, and vC05, respectively). **f** The proportions (%) of different vascular subtypes in subcutaneous (sc), omental (om),

and perivascular (pv) WAT depots. **g** The proportion of vC06 and vC08 in sc and om depots was supported by deconvolution of bulk transcriptomic data from Arner et al.³² (upper panel) and Krieg et al.³³ (lower panel). *p* values were calculated by two-sided Wilcoxon signed-rank test. EC endothelial cells, VSMC vascular smooth muscle cells. Source data are provided as a Source data file.

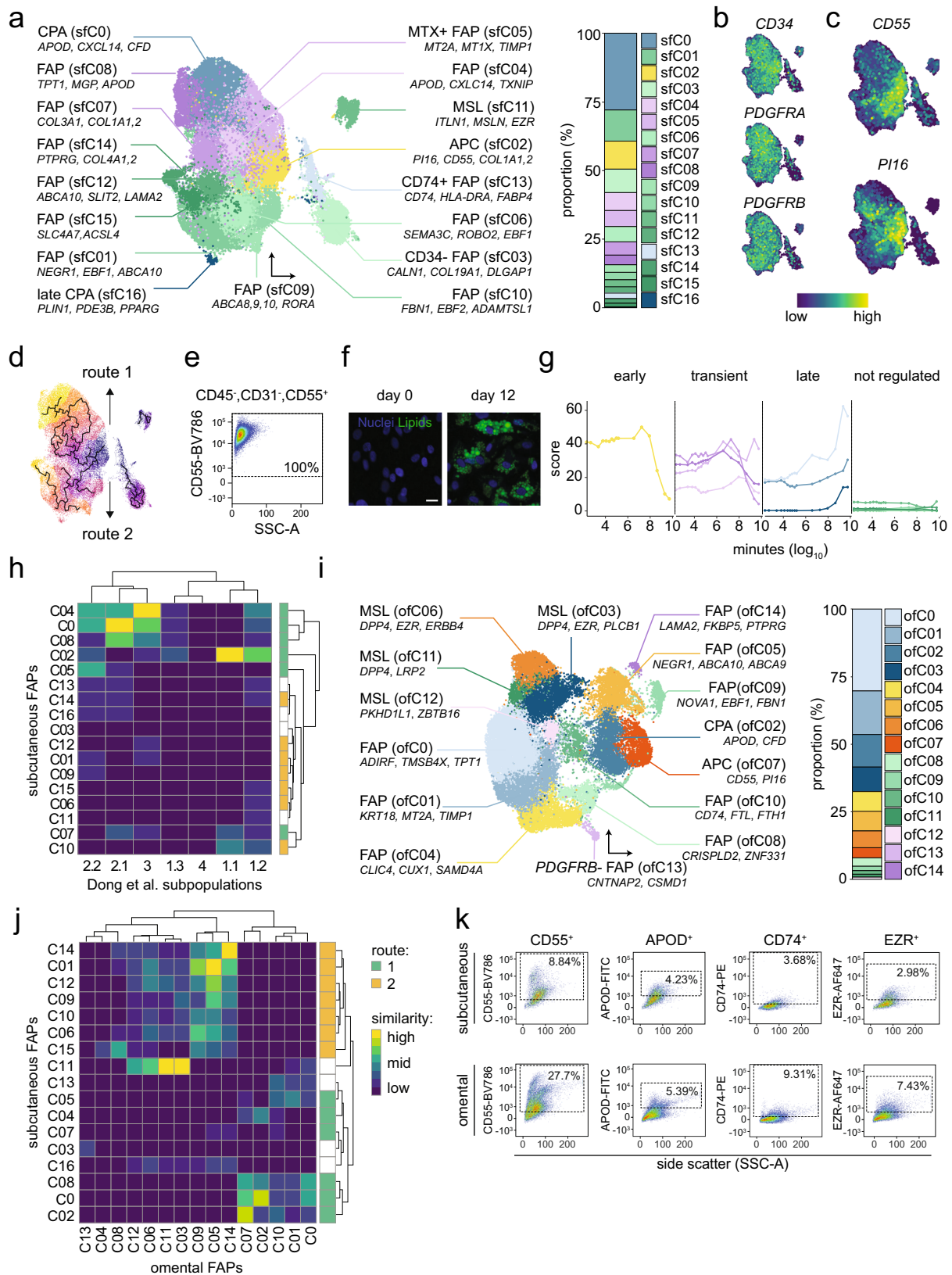
Omental and subcutaneous FAP signatures largely overlap

The omental FAPs separated into 15 clusters (ofC0-14) (Fig. 4i, Supplementary Data 2). To annotate these, we compared their signatures to subcutaneous FAPs. We found that several cell populations shared overlapping marker genes between depots (Fig. 4j, Supplementary Fig. 4c–d). Thus, *CD55/PI16*-expressing adipose precursors (sfC02) matched ofC07, and *APOD/CFD*-expressing committed preadipocytes (sfC0) corresponded to ofC02. All FAPs in route 2 showed strong similarities to three omental clusters (ofC05, ofC09, and ofC14). *CD74* was highly enriched in sfC13 and ofC10 (Supplementary Fig. 4d), but the overall Jaccard index between these two cell types was modest. The mesothelial-like cell signature in subcutaneous WAT (sfC11) was recapitulated in multiple omental FAPs (ofC03, ofC06, and ofC11–12). Of note, *DPP4* was enriched in these omental clusters, but not in the corresponding subcutaneous cells, indicating that this gene marks different subsets of FAPs in the two depots (Supplementary Fig. 4c), a notion previously suggested in mice⁴⁴. Flow cytometric analysis of subtype-specific surface markers in the stromal vascular fraction of WAT biopsies from subcutaneous and omental WAT confirmed the presence of sf02/ofC07 (*CD55*⁺), sfC0/ofC02 (*APOD*⁺), sfC13/ofC10

(*CD74*⁺) and mesothelial-like cells (*EZR*⁺) in both depots (Fig. 4k, Supplementary Fig. 4d). We did not find any expression profiles similar to the fibro-inflammatory progenitors previously described in mouse epigonadal WAT⁴ (Supplementary Fig. 4e). Data from the perivascular depot separated into eight clusters (pf0–pf07) (Supplementary Fig. 4f). While pfC0 resembled ofC07 (adipose precursors) and ofC12, pfC03 was linked to ofC02 (committed preadipocytes). The remaining clusters did not display strong similarities to any of the other FAP subtypes identified in subcutaneous WAT.

Adipocytes display inconsistent heterogeneity between studies

In contrast to scSeq, snSeq allows for analyses of mature adipocytes. In the present study, we analyzed snSeq datasets from subcutaneous (*n* = 4), omental (*n* = 2), and perivascular (*n* = 1) fat depots. As with the other cell classes, we jointly analyzed objects classified as fat cells first. However, this resulted in poor ARI, kBET, and LISI indices (Fig. 1e, Supplementary Fig. 2b), suggesting that complete data integration was not possible to achieve between studies and depots (Supplementary Fig. 5a). As a next step, we analyzed the depots separately. This, however, did not improve our integration as most clusters separated



according to studies rather than biological similarities between datasets (Supplementary Fig. 5b).

A possible reason for incomplete data integration is that there are few common features between studies, even in the low-dimensional space²¹. To test if data harmonization was influenced by a limited degree of overlap, we next analyzed the studies individually. We

focused on data produced by Emont et al.⁹ and our own results (Massier et al. #1) generated in subcutaneous WAT as they contain the largest number of subjects and objects. We selected the top 50 marker genes for all clusters and found that adipocytes displayed lower fold-changes compared to the other cell classes (Fig. 5a, left panel). This indicates that the degree of cell heterogeneity is less pronounced in

Fig. 4 | FAPs display different levels of commitment in human WAT.

a Nomenclature and proportions for subcutaneous FAPs (sfCO-16) including a UMAP with selected marker genes (left panel) and a stacked bar chart displaying the proportion (%) of different subtypes in subcutaneous white adipose tissue (WAT) (right panel). **b, c** Selected FAP marker gene expression profiles displayed in UMAPs. **d** Pseudo-time trajectory analysis initiated from the *CD55/PII6*-enriched cell cluster (sfCO2). Two main trajectories were discovered: route 1 (upper) and route 2 (lower). **e–g** *CD55*⁺ positive human adipose-derived stem cells were **e** analyzed by flow-cytometry and **f** imaged before/after adipogenic induction in vitro. Nuclei are stained by Hoechst (blue) and lipid droplets by BODIPY (green). Experiment was repeated three times with similar results. Scale bar is 20 μ m. **g** deconvolution of bulk RNAseq data from these cells shows how the expression of marker genes for

FAP subtypes in panel **a** vary during adipogenesis (colors are matched in **a** and **g**). **h** Heat map displaying similarities (Jaccard index) of gene expression profiles between inguinal WAT from mice (P1.1 to P4) and subcutaneous FAPs (sfCO-16). Note that human cells displaying overlap with mouse FAPs are only found in route 1. Explanatory legend is visualized in **j**. **i** Same as **a**, but for omental FAPs (ofCO-14). **j** Same as in **h**; but for comparisons of subcutaneous and omental human FAPs. **k** Flow cytometric analysis of *CD55*⁺, *APOD*⁺, *CD74*⁺, and *EZR*⁺ FAPs from stromal vascular cells (*CD45*⁺, *CD31*⁺ and *CD34*⁺) of subcutaneous and omental WAT, respectively. Percentages represent the frequency of all gated live single cells in the representative sample. APC adipose precursor cell, CPA committed preadipocytes, FAP fibroblast and adipogenic progenitor cells, MSL mesothelial-like cells. Source data are provided as a Source data file.

adipocytes. However, there may still be consistencies between the studies. We, therefore, transferred cell type classifications between datasets. In comparison with the other cell types where marker genes displayed clear enrichments and overlap between studies, we found a low overlap and a limited set of reproducible adipocyte marker genes across studies (Fig. 5a, right panel). These included a cluster of genes encoding proteins involved in lipid metabolism e.g., *ABCD2*, *ACACB*, *CD36*, *DGAT2*, *GPAM*, *HACD2*, and *LPL* (Fig. 5b).

Because of the modest heterogeneity and low reproducibility across studies of adipocytes, we benchmarked the snSeq data and our recently published STx-based results⁷ against rRNA-depleted⁴⁵ and cap-trapped⁴¹ bulk RNAseq of isolated human mature fat cells. This revealed that the STx data were positioned close in space to the bulk results, while all snSeq datasets clustered together with considerably fewer similarities to the other samples (Fig. 5c, upper panel). To test the reproducibility of these results, we generated snSeq, STx, and bulk RNAseq from the same individual and repeated the analyses. This confirmed that STx correlated better with bulk RNAseq data than snSeq (Fig. 5c, lower panel). We characterized this further by using the FANTOM5 expression atlas⁴⁶, where we identified 218 transcripts that were enriched at least 50-fold in adipocytes compared to other cell types (Supplementary Fig. 5c). These genes included multiple established adipocyte markers and we analyzed their expression levels in data from the three platforms (Fig. 5d). We observed marked variations in the expression between methods. By filtering based on genes that displayed a high discordance ($>5 |\Delta_{z\text{-scores}}|$) between snSeq and STx, we found that several STx adipocyte subpopulation marker genes were less expressed or not detected by snSeq, but highly abundant in bulk RNA and STx data (Fig. 5e, Supplementary Fig. 5d). These included marker genes of previously described⁷ adipocyte subtypes (Fig. 5e). Conversely, *PPARG*, *WDFPCP*, and *PDE3B* were higher in snSeq. These types of platform-specific biases may contribute to the low reproducibility and heterogeneity scores as has been shown previously for adipocytes⁴⁷. In subsequent analyses, we, therefore, pooled the adipocyte snSeq data into one class.

Multiple FAP-related signals target M2-like macrophage subpopulations

Having defined cell types present in WAT through our meta-map, we inferred their communication routes using *CellChat*⁴⁸. We first summarized the expression of ligands *vs.* receptors across the different cell types and next identified specific cell-cell interactions via ligand-receptor patterns in the subcutaneous and omental depots (Fig. 6a, b, Supplementary Fig. 6a). Our analysis suggested that FAPs were mainly relaying information, which in turn was primarily received by M2 macrophages. Clustering of pathways by functionality allowed us to link these FAP-myeloid communication routes to for example complement, chemerin, and IL16 signaling (Supplementary Fig. 6b). Another striking finding was that Mox (myC15), which are only present in subcutaneous WAT and characterized by exceptionally high expression levels of various pro-inflammatory cyto- and chemokines (Fig. 6c), both relayed and received CCL, CXCL and TNF signals. Thus,

these cells received CCL5 input from different *CD8*⁺ T cells (in particular *lyCO2-03*) via *CCR1*, and signaled to vascular cells (*vCO1* and *vC11*) via ligands (*CCL2*, *CXCL2*, *CXCL8*) recognized by *ACKR1* (Fig. 6d). For TNF, Mox signaled to adipocytes and myeloid cells via *TNFRSF1A*, and to *CD8*⁺ T cells/NK cells (*lyCO3*, *-06*, *-09*) and endothelial cells (*vCO1-03*) via *TNFRSF1B* (Fig. 6d). The validity of these *in silico* analyses was supported by the observation that, the *KIT* receptor was only present in mast cells⁴⁹ while periostin was solely relayed from pericytes⁵⁰ (Supplementary Fig. 6c).

Spatial distribution of FAPs suggest distinct adipogenic niches

To add a spatial dimension to our meta-map, we re-analyzed previously generated STx data of subcutaneous human WAT from ten individuals⁷ using six deconvolution tools: *DestVI*, *stereoscope*, *Tangram*, *RCTD*, *cell2location* and *SPOTlight*. Although all six frameworks provided similar results (Supplementary Fig. 7a), we opted to use *cell2location* as it has been shown to be a robust deconvolution tool¹⁷. In contrast to FAPs, lymphocytes, and adipocytes, we found that vascular and myeloid cells were concentrated in specific areas of the tissue (Fig. 7a). For the latter, these regions included classical monocytes (myC14) and M1-like macrophages (LAMs [myC02], Mmes [myC10] and Mox [myC15]) but were devoid of M2-like macrophages (Fig. 7a). We confirmed clustering of LAMs in specific areas of WAT by immunofluorescence (Fig. 7b), thereby confirming previous findings in mice⁶. To complement these studies, we systematically identified within-spot colocalization patterns. For this, we correlated deconvolution scores for each cell type across all spots and identified three clusters (Fig. 7c, Supplementary fig. 7b). These included endothelial cells as well as two groups of FAPs. Further analyses showed that one FAP subtype (sfC12) was enriched in areas close to endothelial cells (Fig. 7d). This contrasted with the other FAPs, which displayed strongly negative relationship to vascular cells. In addition, another FAP subtype (sfC08) was found close to LAMs (myC02) (Fig. 7d). These associations were present in multiple individuals (Supplementary Fig. 7c) and were confirmed by immunofluorescence (Fig. 7e). Altogether, this suggests that FAPs have specific tissue distributions, possibly to form different types of adipogenic niches.

Two clusters of cells are reciprocally associated with metabolic health

A major weakness of most transcriptional studies with single-cell resolution is that the clinical relevance of the identified cell types is difficult to determine. To address this limitation, we used single-cell marker genes to deconvolve subcutaneous WAT bulk transcriptomic data from eight independent studies comprising a total of 864 individuals. As displayed in Fig. 8a and further detailed in Supplementary Table 3, together these cohorts included both adult men and women with a broad range in age, BMI, waist-to-hip ratio, circulating triglycerides, HDL-cholesterol, and leptin levels as well as insulin sensitivity estimated by *HOMA_{IR}*. We also retrieved data on fat cell volume and lipolysis (basal and isoprenaline-stimulated), which are two measures linked to metabolic health⁵¹. By clustering the correlations between cell

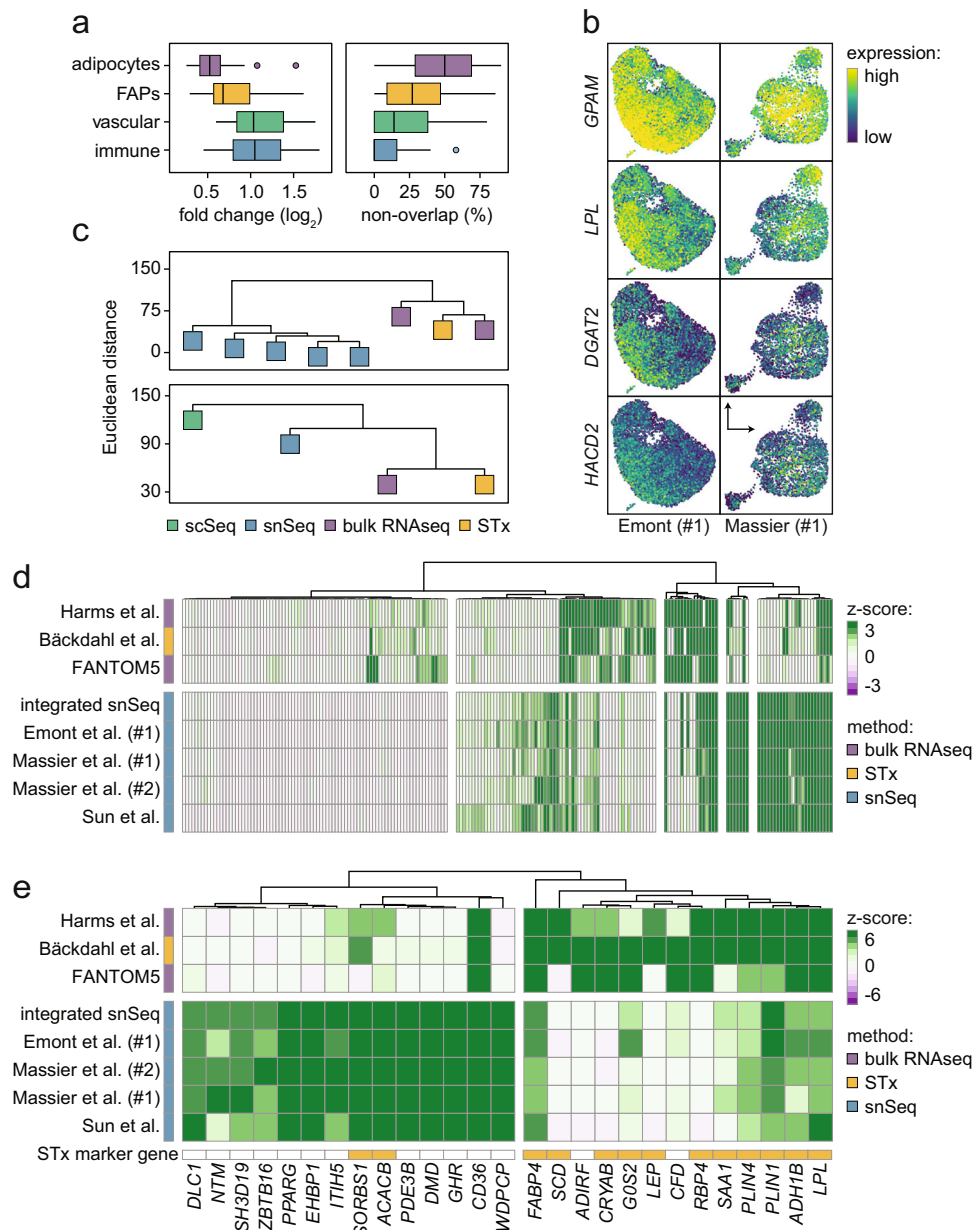


Fig. 5 | Adipocyte snSeq data display inconsistent marker gene overlaps in WAT. **a** Single-nucleus sequencing (snSeq) data from Emont et al. (#1) and Massier et al. (#1) were analyzed according to top marker genes for adipocytes, FAPs, vascular, and immune cells, respectively. In comparison with other cell classes, adipocyte marker genes displayed lower fold-changes (left panel) and a limited overlap (right panel). **b** Representative examples of adipocyte marker genes in subcutaneous WAT displaying overlap between the indicated studies. **c** Dendrograms of snSeq, bulk RNAseq of isolated mature adipocytes (from the

FANTOM5 atlas^{46,81} and Harms et al.⁴⁵) and spatial transcriptomics⁷ (STx) (upper panel). Comparisons of scSeq, snSeq, bulk RNAseq, and STx data of subcutaneous white adipose tissue from the same individual (lower panel). **d** Heatmap of adipocyte marker genes with a >50-fold enrichment in adipocytes vs. other tissues included in the FANTOM 5 atlas. Results are shown for each study as well as for the combined snSeq data after integration. **e** Same as in **d**, but for genes with discordant expression ($|\Delta z\text{-score}| > 5$) comparing STx and snSeq data. Source data are provided as a Source data file.

types and the mentioned parameters, we identified major trends in the data. Thus, while cluster A included six cell types that associated positively with a metabolically beneficial profile, cluster B contained 15 cell types that correlated negatively with the same parameters (Fig. 8b). Cluster C included 37 cell types which displayed weaker links to metabolic states. Of note, age was not associated with any specific cell type (Fig. 8b).

In more detailed analyses, we found that cluster B was over-represented by immune cells, e.g., LAMs (myC02), Mmes (myC10), DC2 (myC03), six out of nine M2-like macrophages (myC0-01, myC07-08, myC11 and myC13), early differentiated CD8⁺ (lyC02) and CD16⁺ NK cells (lyC06) (Fig. 8b, c). These results are in line with previous data

demonstrating that specific immune cell subtypes are enriched in states of insulin resistance and obesity¹. In contrast to cluster B, cluster A enriched for FAPs and vascular cells (Fig. 8b, c). The latter included blood endothelial capillary cells (vC0) and could be due to capillary rarefaction, a phenomenon characterized by reduced capillary beds previously reported in WAT from people with obesity⁵². For FAPs, we observed that *CD55/PI16*-expressing adipose precursors (sfC02) were the only cells present in cluster B while some intermediate/late states (sfC04, -14, and -16) were found in cluster A. This suggests that adipogenesis may be impacted by metabolic health at several different levels. To reveal associations between adipocytes and clinical measures, we used STx marker genes as this platform reflects the

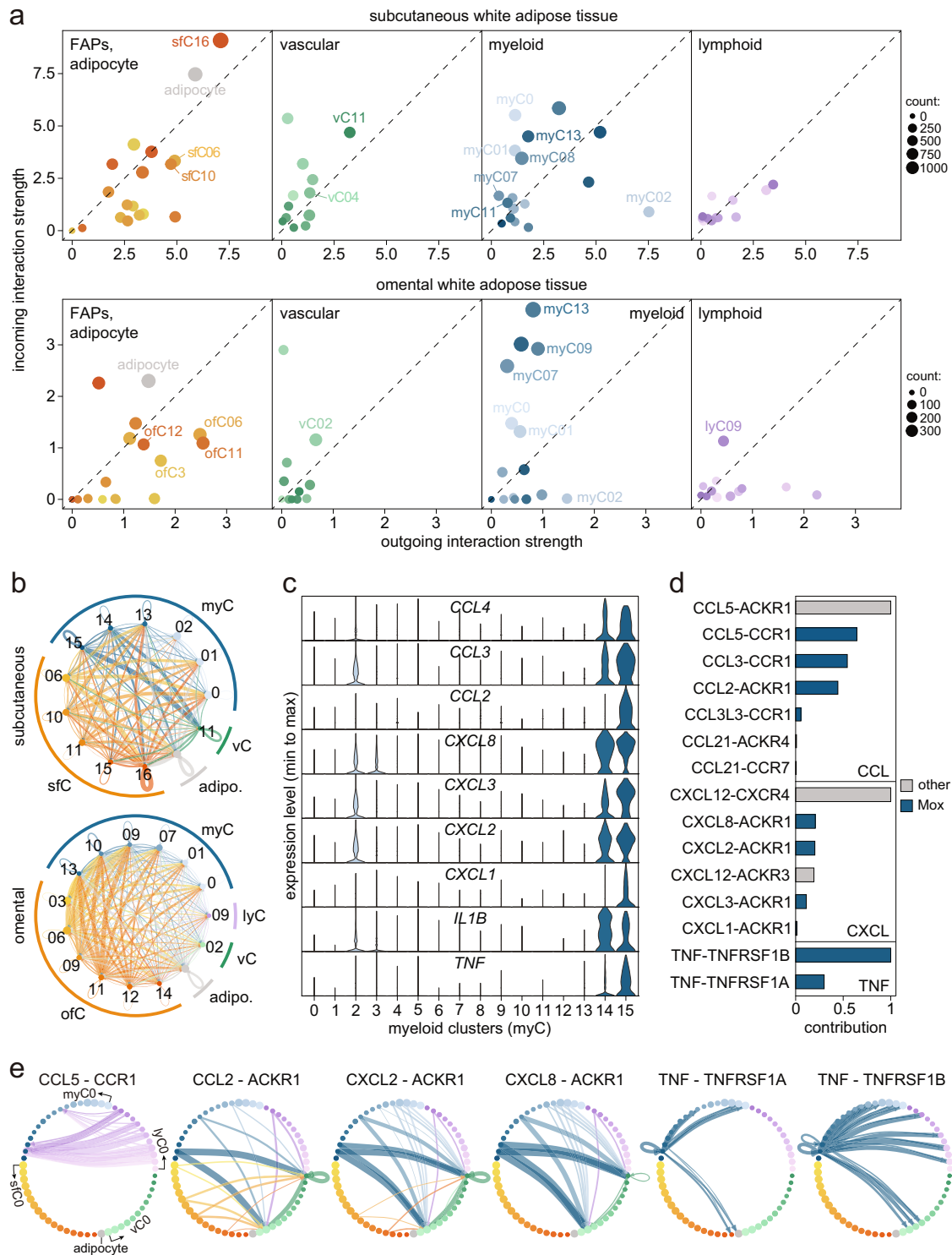
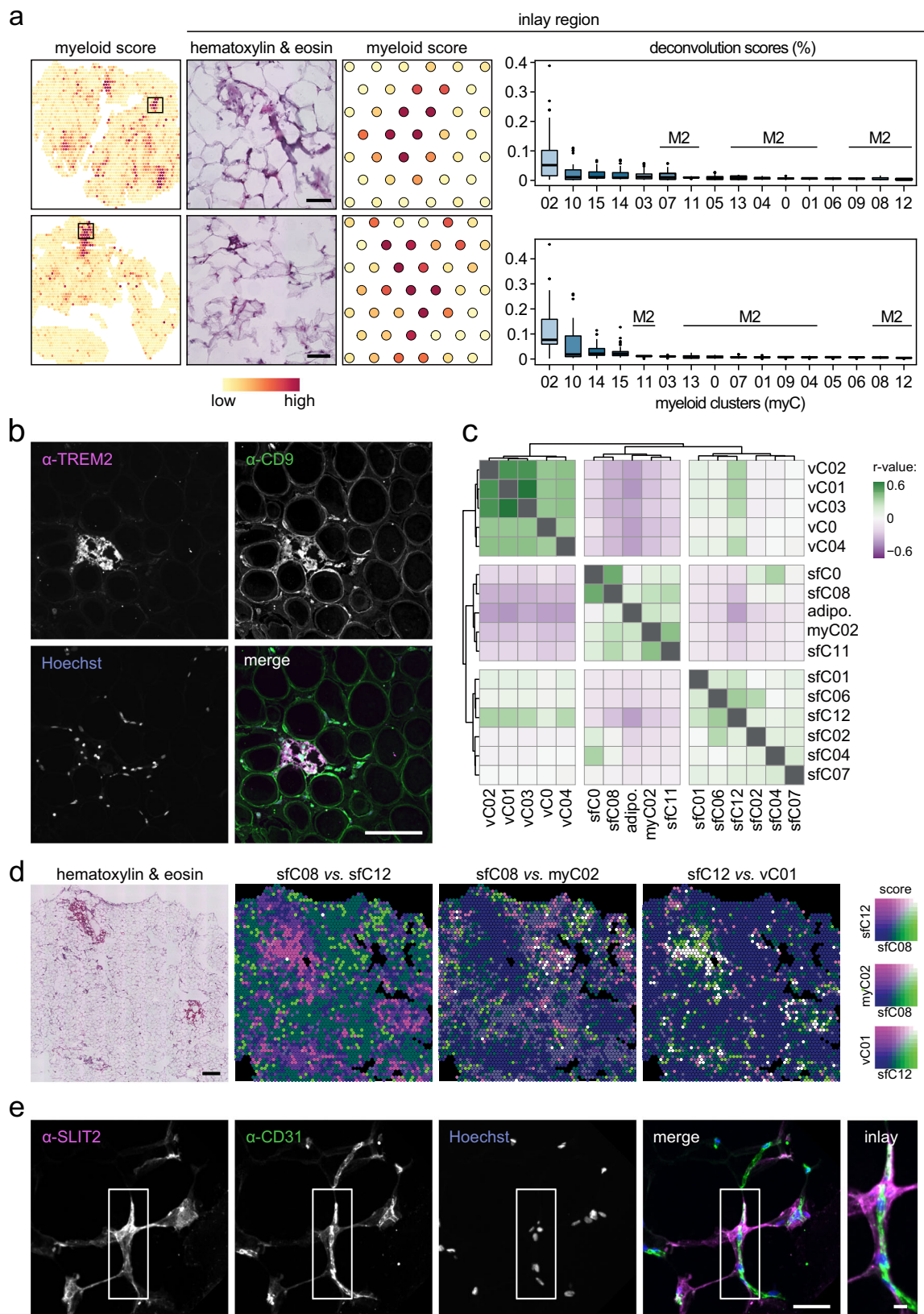


Fig. 6 | FAPs send multiple signals which are received by M2-like macrophages. **a** Incoming and outgoing interaction strengths for FAPs/adipocyte, vascular, myeloid, and lymphoid cells in subcutaneous (upper panels) and omental (lower panels) WAT. Selected cell types are indicated. **b** Subcutaneous (upper) and omental (lower) cell-cell communication predictions for clusters identified in Supplementary Fig. 6a. Lines indicate interactions between cell types where the strength is proportional to the line width and the color defines the sending subpopulation. **c** Violin plots for selected marker genes enriched in the Mox cluster

(myC15). **d** Contribution of each ligand-receptor (L-R) pair to the overall cell-cell communication strength. Blue bars are strongly contributed by Mox (myC15). **e** Predicted cell-cell interactions for the indicated L-R pairs. Line widths and colors indicate signaling strengths and sending subpopulations, respectively. Cell types are in numerical order as shown in the left-most panel. Note that the myeloid and lymphoid clusters end with mast cells and B cells, respectively. Source data are provided as a Source data file.



transcriptional profiles of adipocytes more closely than snSeq. In concordance with previous results obtained in a small cohort⁷, we found that Adipo^{PLIN} correlated negatively with BMI, insulin resistance and circulating leptin levels while Adipo^{LEP} was positively associated with all these measures (Supplementary Fig. 8a). In contrast, Adipo^{S44} displayed weak correlations with all investigated parameters.

Finally, to test if clusters A and B were impacted by weight changes induced by bariatric surgery, we retrieved WAT transcriptomic data from two of the studies where subjects were followed two and five years post-operatively ($n = 52$)^{53,54}. Our results revealed that in both cohorts, clusters A and B were stable and normalized by weight loss (Fig. 8d, Supplementary Fig. 8b). One exception was blood endothelial

Fig. 7 | WAT contains niches populated by specific sets of cells. **a** Representative sections from two subjects displaying areas densely populated by myeloid cells (left panels). The indicated regions are magnified where the hematoxylin & eosin stain is shown in the middle and the Visium slide myeloid score is shown. Deconvolution scores for myeloid subpopulations in the inlay regions are shown in the right panels. Boxplots are presented as interquartile range plus median and Tukey whiskers; scale bar is 100 μm . **b** Representative immunostaining of human subcutaneous white adipose tissue incubated with antibodies targeting LAM marker proteins TREM2 and CD9, respectively. Nuclei were stained with Hoechst. The experiment was repeated three times with similar results. Scale bar is 100 μm .

c Pair-wise correlation heatmap displaying within-spot associations between cellular subpopulations. Full heatmap is shown in Supplementary Fig. 7b. **d** Representative sections displaying the distributions of selected subpopulations of FAPs (sfCO8 and -12), myeloid (myCO2), and vascular cells (vCO1). Scale bar is 500 μm . **e** Representative immunostaining of human subcutaneous white adipose tissue incubated with antibodies targeting the sfC12 marker protein SLIT2 as well as the endothelial protein CD31. Nuclei were stained with Hoechst. The experiment was repeated seven times with similar results. Scale bar is 50 μm in the merged panel and 10 μm in the inlay. Source data are provided as a Source data file.

capillary cells (vCO), which remained unaltered by weight loss (Fig. 8e). These data⁵³ also allowed us to assess effects of weight regain comparing follow-ups at two and five years. As displayed in Supplementary Figure 8c, subdividing subjects into tertiles based on long-term weight regain or stability showed that except for vCO, several cell subtypes followed the changes in body weight. Altogether, these observations suggest that the cellular landscape of WAT is dynamic and mirrors alterations in fat mass.

Discussion

Our meta-analysis integrates existing and newly generated single-cell data with bulk sequencing of *in vitro* adipogenesis and intact WAT from large clinical cohorts. By overlapping this with spatial transcriptomics and data from human and murine single-cell resources generated in different organs, we provide a meta-map of cell types and their spatial organization in human WAT. Altogether, this allowed us to define >60 distinct cell types including immune cells with diverse activation states, intermediate vascular cell types with hybrid transcriptional profiles, and FAPs displaying distinct tissue localization and different levels of adipogenic commitment.

To create a cellular nomenclature across adipose depots, we included data from subcutaneous, omental, and perivascular WAT in our meta-analysis. Based on depot comparisons, we found that although proportions differed, most cell subpopulations were present in all three regions. This was also true for FAPs, even though they have been suggested to contribute to depot-specific differences in tissue growth. For example, both adipose precursors and committed pre-adipocytes were found in all three sites. However, within subcutaneous WAT, the FAPs displayed distinct localizations where some were found close to vessels and others were adjacent to specific macrophages. The latter is of interest given that our ligand-receptor analyses suggested that FAPs relayed multiple signals to myeloid cells. Apart from these quantitative and microarchitectural aspects, we also observed that a limited number of cell types were unique to either region, including Mox and a few M2-like macrophage subtypes. Although we corroborated these results by deconvolving bulk transcriptomic data from paired samples of subcutaneous and omental WAT, they need to be validated in additional cohorts and the function of these cells needs to be determined. In addition, the spatial analyses presented herein were only performed in subcutaneous WAT and should be followed-up in other depots.

In our meta-analysis, adipocytes comprised ~20% of the WAT cell population and displayed a transcriptional fingerprint that was distinct from FAPs, immune and vascular cells. However, in contrast to these cell classes, adipocyte data were exclusively generated using snSeq and the results displayed less pronounced and reproducible heterogeneity between studies. A possible reason for this lack of consistency is that snSeq preferentially detects nascent and long transcripts⁴⁷. This is further supported by our benchmarking of technical platforms where snSeq data, in comparison to STx results, associated poorly with the transcriptional signature of isolated fat cells. In fact, numerous adipocyte subtype marker genes identified by STx (e.g., *LEP*, *PLIN4*, *SAA1*, *RBP4*)⁷ were not, or very weakly, detected by snSeq. We therefore conclude that combined analyses using

different technical platforms are required to confidently identify adipocyte subtypes.

Although we have combined studies to obtain data at the single-cell level from approximately 100 samples, we have not determined the influence of age, anthropometric measures, and disease states on these results. Instead, we created a cartography of cells present in WAT and used this framework to deconvolve bulk transcriptomic results from over 860 samples. This expands previous efforts^{55,56} and allowed us to link the identified cell populations to multiple clinical and WAT parameters. More specifically, we show that *CD55/PLI6*-expressing adipose precursors as well as a large set of immune cells, including LAMs and Mmes, were enriched in individuals with markers of a pernicious metabolic phenotype, i.e., subjects with large fat cell volume, high waist-to-hip ratio, high HOMA-IR and impaired lipid mobilization. Conversely, a group of intermediate FAPs and capillary endothelial cells associate negatively with the same parameters. Additional analyses in cohorts before and after bariatric surgery, revealed that multiple cell clusters enriched in people with obesity and insulin resistance are normalized upon weight loss. Together, these data extend previous results on WAT expansion by confidently identifying specific cell types linked to increased inflammation as well as attenuated adipogenesis and vascularization. Nevertheless, a limitation with the present work is that we did not investigate longitudinal data following other types of interventions including, life-style-related changes, and/or pharmacological treatments.

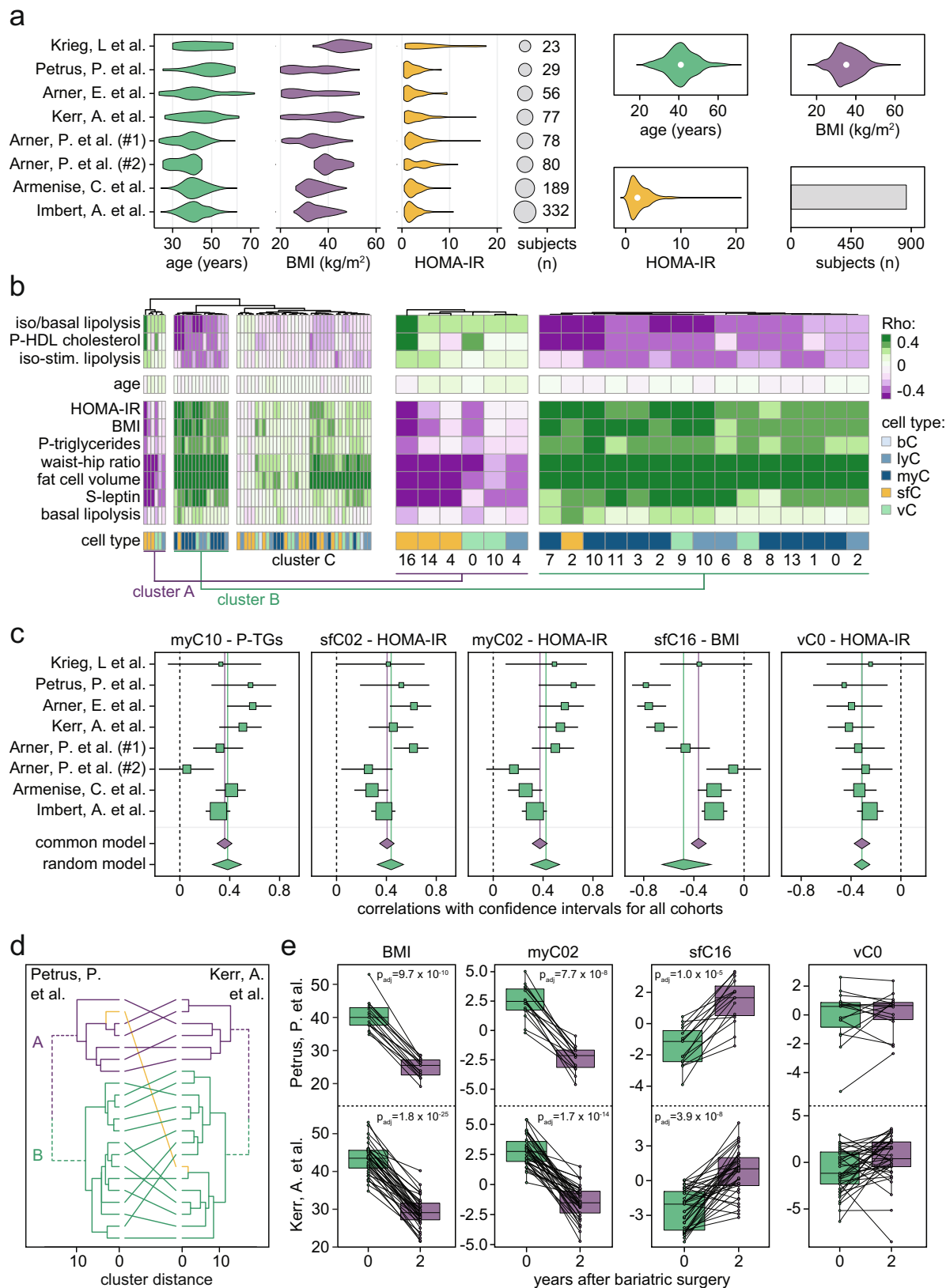
Taken together, in this meta-analysis of 17 datasets and >800 bulk transcriptional profiles from eight clinical studies, we have comprehensively defined the cellular composition of human WAT in health and metabolic disease. Thus, by jointly analyzing data from multiple types of studies, we have created a framework that is easily accessible and includes additional tools for WAT analyses such as new models in *CellTypist*. We, therefore, provide a rich resource to facilitate future studies of specific WAT-resident cell types in relation to aspects not investigated herein, such as ethnic differences and the impact of therapeutic interventions.

Methods

Clinical studies

Inclusion and Ethics. This study was performed in agreement with the Declaration of Helsinki. Studies of cohorts presented for the first time herein (Massier et al. #1–4), were approved by the regional ethics boards in Stockholm (clinical trials identifiers: NCT01785134 and NCT01727245) and Leipzig (approval numbers: 159-12-21052012 and 004/21-ek) and explained in detail to each participant who gave informed written consent. For retrospective analyses of published data, the studies have been approved by the respective ethical boards where informed written consent was obtained from all participants. For data detailed in Fig. 8d, e, primary outcomes for both clinical trials (NCT01785134 (DEOSH) and NCT01727245 (NEFA)) have been described at clinicaltrials.gov and previously published^{7,53,57–59}, and the studies have been completed.

Sample collection and preparation. Samples of cohort 1 and 3 were collected in Stockholm (Sweden) and processed by T.W. in Zürich



(Switzerland). Adipocyte nuclei were isolated following a modified nuclear isolation protocol⁶⁰. In total, 50 mg of fresh or frozen WAT was first minced into 1–3 mm pieces and then homogenized on ice in 0.1% CHAPS in CST buffer supplemented with 0.2 U/ μ l RNAase inhibitor (RI) using a Dounce homogenizer. After homogenization, samples were left on ice for five minutes following which PBS supplemented with BSA

and 0.2U/ μ l RI was added to obtain a final concentration of 1% BSA. The lysates were filtered through 40- μ m cell strainers and centrifuged at 500 \times g for five minutes at 4 °C. The nuclei pellets were resuspended with 1% BSA in PBS supplemented with 0.2 U/ μ l RI and centrifuged again at 50 \times g for five minutes at 4 °C. This step was repeated once more. After the final resuspension, nuclei were filtered through 20- μ m

Fig. 8 | Deconvolution of transcriptomic data reveals cluster-specific clinical associations. **a** Bulk transcriptomic data from eight cohorts were retrieved, the distribution in age, BMI, and HOMA-IR are shown in the left panel. Summary statistics are detailed in the right panels. **b** Heatmap displaying the association between individual cell types (denoted by numbers and color according to the classification in Figs. 2–4) with: anthropometric measures, HOMA-IR, circulating levels of HDL-cholesterol, triglycerides, and leptin (all in the fasted state), fat cell volume as well as adipocyte lipolysis (basal, isoprenaline-stimulated and isoprenaline-stimulated/basal). Three main clusters (A–C) were identified where cluster A and B are magnified in the right panel. **c** Representative Forest plots displaying the associations between individual measures and cell types. Data are shown as

correlations with 95% confidence intervals for each study and summarized using both common and random effects models. For all displayed data, p values were <0.0001 . **d** Stability of clusters A and B were determined in the two indicated cohorts where WAT bulk transcriptomes were generated before and two years following bariatric surgery. **e** Effects of weight loss induced by bariatric surgery in two cohorts. Panels display deconvolution scores for the indicated cell subpopulations. p values were calculated by two-sided paired sample t test ($n = 15$; Petrus et al.⁵⁴ and $n = 37$; Kerr et al.⁵³) and boxplots are presented as interquartile range plus median and Tukey whiskers with individual, paired data points. Source data are provided as a Source data file.

cell strainers and loaded directly on a 10X Chip G. 10X-libraries were prepared with the Chromium Single-Cell v3.1 reagent kit following the manufacturer's protocol (10X Genomics). Suspensions containing around 1200 nuclei per μl were loaded on Chip G followed by reverse transcription to obtain cDNA, which subsequently was amplified and used for library construction. After preparation, the libraries were sequenced on a NovaSeq 6000 platform (Illumina). For data analysis, the human genome assembly GRCh38.p13 was used. Mapping was performed using 10x Genomics *Cell Ranger* (v6.0.2). *CellBender* (v0.2.0)⁶¹ was used on 'raw_feature_bc_matrix' to remove empty droplets and ambient RNA; *scDblFinder* (v1.5.11)⁶² was applied to exclude potential doublets. Downstream analyses were performed as all other included studies (see below).

Samples of cohort 2 and 4 were collected and processed in Leipzig (Germany) by P.A.N.N. Paired samples of omental and subcutaneous WAT were obtained from female patients with obesity undergoing different bariatric surgery procedures (Roux-en-Y Gastric Bypass and sleeve gastrectomy). After collection, samples were washed using PBS, placed on ice until the end of the surgery procedure, snap-frozen in liquid nitrogen and stored at -80°C for later use. Sequencing analyses were performed on isolated nuclei as detailed above. Single-nuclei RNAseq libraries were generated using the Chromium Single Cell 3' v3 assay (10x Genomics) and sequenced with NovaSeq 6000 S4 flow cell platform (Illumina). Raw reads were aligned to the human genome (hg38) and cells were called using 10x Genomics *Cell Ranger* (v.6.0.1).

Collection of publicly available datasets. Peer-reviewed WAT datasets containing either snSeq, scSeq or STx with publicly available results published until 31.03.2022 were included in the present meta-analysis (Supplementary Table 1). If not present in the published articles, the corresponding authors were contacted by email to obtain information regarding sample numbers and gender as well as ranges of age and BMI.

Re-analysis of publicly available datasets. Publicly available datasets were re-analyzed with *Seurat* v4.1.0¹⁶ in R v4.1.2⁶³ (pipeline available via GitHub [https://github.com/lmassier/hWAT_singlecell]). Mitochondrial and hemoglobin genes, as well as further confounding transcripts, including *MALAT2* and *NEAT1*, were removed prior to analysis. All data were normalized using *scTransform*⁶⁴ and corrected for subject effects using *Harmony* v0.1.0²⁵ before performing independent component analysis⁶⁵. Clusters were determined using *FindNeighbors* and *FindClusters* in *Seurat* after generating Uniform Manifold Approximation and Projection (UMAP) data projections using *RunUMAP*⁶⁶. Spatial data were analyzed as described recently⁷.

Cluster classification and annotation. Cluster classification for individual cohorts was assisted by a supervised network analysis where each cell cluster was represented as a node. Nodes were connected by edges by calculating overlap percentages of positively enriched marker genes (FDR-adjusted p value <0.05). Minimum requirements for edge connections were $>15\%$ genes overlapped in one of the two nodes and $>5\%$ in both nodes. Based on this, Jaccard similarity scores were

calculated, and edges were created based on the five highest values. The network was built in R v4.1.2. using *igraph* v1.2.11 and visualized in Cytoscape 3.7.1 using *Rcy3* v2.14.1⁶⁷. Integrated cluster annotations were performed manually using multiple reference datasets (Supplementary Table 2).

Data integration and benchmarking

We evaluated the following integration tools: *rPCA* provided with *Seurat*¹⁶, *Harmony*²⁵, *BBKNN* as well as *scVI*. In addition to identification/clustering of prominent marker genes in the integrated data, benchmarking included calculations of ARI coefficients, LISI scores, kBET acceptance rates (1- rejection rate) for integration across methods, depots and cohorts. ARI was calculated using the *adj.rand.index* function in *pdfCluster* v1.0-3 by supplying factors of either depots, methods or cohorts in addition to the identified clusters. Average LISI scores were estimated using *lisi* v1.0 *compute_lisi* command adding embeddings of the UMAPs along the meta data. kBET scores were calculated using *kBET* v0.99.6 and the respective integrated reductions (e.g., *Harmony* or *scVI*) in the *Seurat* object. Data from different depots or methods within the same study were treated as independent cohorts, which was used as batch variable to integrate over, thereby correcting for differences in methods and sequencing platforms. Of note, all cohorts except for Acosta et al.¹² ($<0.5\%$ of analyzed cells), were sequenced in 3' direction, thereby facilitating integration (Supplementary Table 1). Guided by our testing, we opted to integrate data individually for adipocytes, FAPs, immune and vascular cells. Based on these results, *scVI* integration using the 2000 most variable features (using *VariableFeatures* in *Seurat*) was applied in the final analysis. *Seurat* objects were transcribed into *anndata* objects using the *sceasy* v0.0.6 function *convertFormat* and *scVI* was run using default settings in R with *reticulate* v1.24 (*setup_anndata*, *SCVI*, *train*, *get_latent_representation*). Subsequent subcluster analyses were performed based on different depots (omental, perivascular, and subcutaneous WAT) or lineages (e.g., myeloid and lymphoid cells). When comparing similarity between individual data sets using Jaccard index, marker genes were selected based on a \log_2 fold-change > 0.5 , and adjusted p value <0.05 .

Deconvolution

Deconvolution of bulk transcriptomic data of human WAT was performed using *BisqueRNA* v1.0.5⁶⁸ using the marker gene approach with a minimum gene count of six. To validate depot differences, two cohorts^{32,33} with available data from omental and subcutaneous WAT were used. We also retrieved sequencing as well as clinical phenotype data from six additional published datasets^{53,54,69–72} (Supplementary Table 3). Deconvolved data were compared in a meta-approach using *Hmisc* v4.6–0 to calculate Spearman correlation and *meta* v5.2–0 to calculate and visualize summarized results using both common and random models⁷³.

Flow-cytometry staining and analysis of data

The procedures for preparing cells for flow-cytometry have been described in detail elsewhere⁷⁴. In brief, stromal vascular fractions

(SVF) were thawed and stained with different antibody combinations prior to analysis with a flow cytometer. Washing steps were performed with wash buffer (PBS supplemented with 0.5% BSA [#A4503, Sigma-Aldrich] and 2 mM EDTA [#E7889, Sigma-Aldrich]) and the cells were centrifuged at $200 \times g$ for 10 minutes. To remove red blood cells, samples were incubated in red blood cell lysis buffer (15.5 mM NH₄Cl, 0.57 mM K₂HPO₄, 0.01 mM EDTA \times 2 H₂O in PBS) for 6 minutes and subsequently washed with wash buffer. Samples were divided into aliquots containing approximately one million cells and subsequently stained with either (i) a lymphocyte antibody cocktail, (ii) an antibody panel for myeloid cells and fibroblasts combined, or (iii) a separate antibody panel for FAPs. The antibody-fluorochrome conjugates used are listed in Supplementary Table 4. Staining with the lymphocyte antibody cocktail was performed by resuspending the cells first in stain buffer (1% FBS, 2 mM EDTA in PBS) with CCR7-APC-Cy7 and incubating for ten minutes at 37 °C. Subsequently, the surface marker antibodies were added to the cell suspension and the incubation was carried out at room temperature for 20 minutes. The cells were washed once with stain buffer, centrifuged at $400 \times g$ for five minutes, and resuspended into $1 \times$ fixation/permeabilization solution (#00-5223-56 and #00-5123-43, eBioscience). After incubating the cell suspensions for 30 minutes at room temperature in the dark, they were washed with permeabilization buffer (#00-8333-56, eBioscience), centrifuged at $400 \times g$ for 5 minutes, and resuspended with an intracellular staining cocktail in $1 \times$ permeabilization buffer for 30 minutes at room temperature in the dark. Lastly, the cells were washed with permeabilization buffer and fixed with 1% PFA (#22023-20 ml, Biotium) for 15 minutes prior to analysis with a BD Symphony analyzer equipped with 355, 405, 488, 561 and 640 nm lasers and DIVA software (BD Biosciences). Fixable live/dead Aqua stain (#L34957, Invitrogen) was included in the surface stain cocktail and used for dead cell exclusion. Gating was performed as outlined in Supplementary Figure 9a. The cells stained with the myeloid panel were incubated in the antibody cocktail for 30 minutes at 4 °C in the dark, washed once with wash buffer, resuspended into flow buffer (0.1% BSA, 2 mM EDTA in PBS), and analyzed immediately with the flow cytometer with a previously set compensation and gating setup. Fixable live/dead yellow dye (#L34968, Invitrogen) was used to exclude dead cells. The gating setup preceding the UMAP analysis is outlined in Supplementary Figure 9b. Cells stained with the FAPs panel were stained in a similar fashion as with the myeloid panel. 7-AAD (#559925, BD Biosciences) was used as live/dead exclusion dye and fluorescence minus one (FMO) controls were used for the gating (Supplementary Fig. 9c). The results were analyzed with FlowJo Software v10.7.1 and v10.8.0 (BD Biosciences). Dimensionality reduction for analyzing the myeloid cells was performed using the UMAP FlowJo plugin v3.1. For this analysis, 1267 myeloid cells from each individual were exported into a new file, barcoded and concatenated. FlowJo Phenograph plugin v3 was applied for unsupervised clustering, with the optimal k-nearest neighbors implemented automatically.

Imaging

Lipid droplet staining before and after adipogenesis. For imaging of CD55⁺ cells before and after adipogenesis, cells were fixed in 4% PFA for 15 minutes at room temperature and washed twice with PBS. Lipid droplets and nuclei were stained with PBS containing BODIPY 493/503 (1:2500, ThermoFisher) and Hoechst 33342 (1:5000, #ab228551, Abcam) for 15 minutes. Cells were then washed four times with PBS and images were acquired using CREST V3 confocal system (Crest Optics) mounted on an inverted Nikon Ti2 microscope equipped with a Prime BSlexpress sCMOS camera (pixel size 6.5 μ m) from Photometrics. A Nikon 20x/0.75 air objective was used to acquire images.

Immunostaining of LAMs (myC02). For immunofluorescence, WAT samples were fixed in cold 4% paraformaldehyde (PFA) for 24 hours,

embedded in paraffin and then sliced into 6 μ m thick sections. Antigens were retrieved by heating up the sections for 20 minutes in 10 mM citrate buffer pH 6.0 (tri-sodium citrate in distilled water) using a microwave. The samples were subsequently washed three times with PBS containing 0.3% Triton X-100 and blocked for one hour at room temperature in PBS containing 0.1% BSA, 0.1% Triton X-100, 50 mM glycine, and 0.05% Tween. Primary antibodies (anti-TREM2 [1:100, #13483-1-AP, Proteintech] and anti-CD9 [1:500, #60232-1-Ig, Proteintech]) were diluted in 0.1% BSA, 0.1% Triton-X-100, 10 mM glycine and 0.05% Tween in PBS and incubated with the sections overnight at 4 °C. This was followed by three wash steps with PBS containing 0.3% Triton X-100 and incubations for 10 minutes at room temperature. After this, slides were incubated with secondary antibodies (donkey α -rabbit conjugated with Alexa Fluor 594 [1:200, #A-21207, ThermoFisher] and donkey α -mouse conjugated with Alexa Fluor 488 [1:200, #A-21202, ThermoFisher]) diluted in 0.1% Tween in PBS for an hour at room temperature. Following three wash steps with PBS containing 0.3% Triton-X-100, 100 μ l Sudan Black B in 70% ethanol was added to each section and the samples were incubated for two minutes at room temperature. The slides were thereafter rinsed in PBS and incubated with Hoechst 33342 (1:10000) diluted in PBS for ten minutes to stain nuclei. Prior to mounting in DAKO Fluorescence mounting media (S302380-2, Agilent Technologies), the samples were washed with PBS and swirled in distilled water.

Immunostaining of FAPs (sfC12) and endothelial cells. Subcutaneous WAT blocks embedded in optimal cutting temperature compound were sliced into 16 μ m thick sections, which were then fixed in 4% PFA for five minutes at room temperature and washed twice with PBS. After this, glycine was added (100 mM final concentration) for ten minutes and slides were blocked for one hour in PBS containing 1% BSA, 0.3% Triton X-100, and 10% normal donkey serum. Subsequently, the slides were incubated overnight in 4 °C with primary antibodies (anti-SLIT2 [1:200, #20217-1-AP, Proteintech] and anti-CD31 1:100, #M082329-2, Agilent Technologies) in incubation buffer containing 5% normal donkey serum, 1% BSA and 0.3% Triton X-100 in PBS. Slides were washed three times with PBS containing 0.3% Triton X-100 for five minutes. They were thereafter incubated with secondary antibodies (donkey α -rabbit conjugated with Alexa Fluor 594 [1:200, #A-21207, ThermoFisher] and donkey α -mouse conjugated with Alexa Fluor 488 [1:200, #A-21202, ThermoFisher]) in incubation buffer for 1 hour at room temperature. Additional washing steps were performed with PBS supplemented with 0.3% Triton X-100. Then, Hoechst 33342 (1:10,000) diluted in PBS was added for 10 minutes to stain nuclei. Prior to mounting in DAKO Fluorescence mounting media, the samples were washed with PBS and swirled in distilled water.

For immunostaining of both myC02 and sfC12/endothelial cells, images were acquired using the NIS Elements software, a CSU-X1 spinning disk confocal (Yokogawa) mounted on an inverted TiE microscope (Nikon) equipped with a \times 1.2 magnification lens and a Kinetix back-illuminated sCMOS camera (pixel size 6.5 μ m QE95%) (Photometrics). A Nikon \times 20/0.75 air objective was used to acquire images.

Bulk RNA sequencing of in vitro adipogenesis

To annotate FAP clusters, we retrieved bulk sequencing data of human subcutaneous adipocyte precursor cells undergoing adipogenesis from four model systems: (i) adipose-derived stem cells⁴¹, (ii) primary SVF-derived cells from subcutaneous WAT⁴¹, (iii) Simpson-Golabi-Behmel (SGBS) syndrome cells⁴², and (iv) human multipotent adipose-derived stem (hMADS) cells⁴³. Scores were generated for each FAP cluster at each timepoint of adipogenesis by calculating expression fold-changes of top 30 marker genes over the background of the respective bulk datasets.

Comparing adipocyte-enriched transcripts between platforms

To identify adipocyte-enriched genes unrelated to single-cell approaches, we retrieved bulk RNAseq data of human isolated subcutaneous adipocytes from the FANTOM5 database⁴⁶. This was compared to pseudobulk data, which was retrieved using *AverageExpression* in Seurat, of both individual snSeq and STx studies, as well as the integrated snSeq data. We calculated transcript fold-changes in these samples compared to the complete dataset. In total, 218 genes with >50-fold enrichment in fat cells compared to all other samples were considered to be adipocyte-enriched. We compared expression levels of these genes between snSeq and STx platforms after z-score normalizing each dataset. As an extra control, we included an additional bulk RNAseq dataset of human isolated subcutaneous adipocytes⁴⁵. By filtering for genes with a $|A_{z\text{-score}}| > 5$, we identified genes with the strongest differences between snSeq and STx.

Spatial deconvolution

We performed *cell2location* v0.1⁷⁵ for deconvolution of STx by using a subset of annotated scRNA-seq data as input. We subsampled the single-cell data set for each cell type according to following criteria: (i) If a cell type had ≤ 1500 cells, select all cells; (ii) if a cell type had >1500 cells, randomly select 1500 cells. We compared *cell2location* with five additional spatial deconvolution methods: *stereoscope* v0.2.0⁷⁶, *SPOTlight* v0.1.0⁷⁷, *RCTD* v2.0.0⁷⁸, *Tangram* v1.0.2⁷⁹, *DestVI* v0.16.2⁸⁰ to validate the robustness of deconvolution results. Default parameter settings were used for deconvolution analysis.

We used spot-wise Pearson correlation between the estimated cell type abundances to quantify cell type colocalization pattern. The Pearson correlations were computed across all spots for each pair of cell types and each subject. High positive correlation indicated that two cell types exhibited similar spatial distributions, while negative correlation suggested distinct spatial distributions between two cell types.

Cell-cell communication analysis

Cell-cell communication analysis was performed using *CellChat* v1.4.0⁴⁸ based on the curated ligand-receptor interaction database (CellChatDB). In brief, subcutaneous and omental normalized gene expression matrices were provided as input to *CellChat*, respectively. The total numbers of interactions and interaction strengths were computed by the *computeCommunProb* function, and the communication probabilities for each cell signaling pathway were calculated by *computeCommunProbPathway* function.

Statistics

As detailed under each subheading above, statistics were performed in R v4.1.2 or GraphPad Prism v9. Data distributions were tested by Kolmogorov-Smirnov and Shapiro-Wilk tests and parametric vs. non-parametric tests were used accordingly. Spearman's rank correlation was used to assess relationship of two continuous variables. For analyses requiring family-wise error rate corrections, p value <0.05 after correcting for false discovery rate using Benjamini-Hochberg was considered significant.

Reporting summary

Further information on research design is available in the Nature Portfolio Reporting Summary linked to this article.

Data availability

Processed data generated in this study have been deposited in the Mendeley database (<https://doi.org/10.17632/y3pxvr4xbf.2>). The raw sequencing data generated in this study have been deposited in the GEO database under the accession code [GSE225700](https://doi.org/10.1101/2023.03.15.532570). The publicly available scSeq and snSeq data re-analyzed in this study were obtained through the GEO database under accession codes: [GSE155960](https://doi.org/10.1101/2023.03.15.532570)¹¹,

[GSE156110](https://doi.org/10.1101/2023.03.15.532570)¹¹, [GSE136230](https://doi.org/10.1101/2023.03.15.532570)¹⁰, [GSE128889](https://doi.org/10.1101/2023.03.15.532570)¹³, [GSE151889](https://doi.org/10.1101/2023.03.15.532570)¹⁴, [GSE128518](https://doi.org/10.1101/2023.03.15.532570)⁶, [GSE164528](https://doi.org/10.1101/2023.03.15.532570)¹⁵, [GSE135134](https://doi.org/10.1101/2023.03.15.532570)⁹, [GSE128889](https://doi.org/10.1101/2023.03.15.532570)⁹ as well as the ArrayExpress database under accession codes: [E-MTAB-9199](https://doi.org/10.1101/2023.03.15.532570)⁸, [E-MTAB-6677](https://doi.org/10.1101/2023.03.15.532570)⁹. Data from Acosta et al. were received after communication with the author. The publicly available RNA sequencing and microarray data of human WAT re-analyzed in this study were obtained through the GEO database under accession codes: [GSE25402](https://doi.org/10.1101/2023.03.15.532570)⁶⁹, [GSE113080](https://doi.org/10.1101/2023.03.15.532570)⁷⁰, [GSE199063](https://doi.org/10.1101/2023.03.15.532570)⁵³, [GSE76399](https://doi.org/10.1101/2023.03.15.532570)³², [GSE59034](https://doi.org/10.1101/2023.03.15.532570)⁵⁴, [GSE141221](https://doi.org/10.1101/2023.03.15.532570)⁷¹, [GSE95640](https://doi.org/10.1101/2023.03.15.532570)⁷². Data from Krieg et al. were retrieved from the original publication [Supplementary Table 7]³³. The data that support the findings of this study are available on request from the corresponding authors [N.M. and M.R.]. Full individual clinical data are not publicly available due to them containing information that could compromise research participant privacy or consent. Source data are provided with this paper.

Code availability

Scripts used for the analyses presented in this study are available at GitHub (https://github.com/lmassier/hWAT_singlecell).

References

- Sakers, A., De Siqueira, M. K., Seale, P. & Villanueva, C. J. Adipose-tissue plasticity in health and disease. *Cell* **185**, 419–446 (2022).
- Shao, M. et al. De novo adipocyte differentiation from Pdgfrbeta(+) preadipocytes protects against pathologic visceral adipose expansion in obesity. *Nat. Commun.* **9**, 890 (2018).
- Schwalie, P. C. et al. A stromal cell population that inhibits adipogenesis in mammalian fat depots. *Nature* **559**, 103–108 (2018).
- Hepler, C. et al. Identification of functionally distinct fibro-inflammatory and adipogenic stromal subpopulations in visceral adipose tissue of adult mice. *Elife* **7**, e39636 (2018).
- Dong, H. et al. Identification of a regulatory pathway inhibiting adipogenesis via RSPO2. *Nat. Metab.* **4**, 90–105 (2022).
- Jaitin, D. A. et al. Lipid-associated macrophages control metabolic homeostasis in a Trem2-dependent manner. *Cell* **178**, 686–698. e614 (2019).
- Backdahl, J. et al. Spatial mapping reveals human adipocyte subpopulations with distinct sensitivities to insulin. *Cell Metab.* **33**, 1869–1882. e1866 (2021).
- Sun, W. et al. snRNA-seq reveals a subpopulation of adipocytes that regulates thermogenesis. *Nature* **587**, 98–102 (2020).
- Emont, M. P. et al. A single-cell atlas of human and mouse white adipose tissue. *Nature* **603**, 926–933 (2022).
- Vijay, J. et al. Single-cell analysis of human adipose tissue identifies depot and disease specific cell types. *Nat. Metab.* **2**, 97–109 (2020).
- Hildreth, A. D. et al. Single-cell sequencing of human white adipose tissue identifies new cell states in health and obesity. *Nat. Immunol.* **22**, 639–653 (2021).
- Acosta, J. R. et al. Single cell transcriptomics suggest that human adipocyte progenitor cells constitute a homogeneous cell population. *Stem Cell Res. Ther.* **8**, 250 (2017).
- Merrick, D. et al. Identification of a mesenchymal progenitor cell hierarchy in adipose tissue. *Science* **364**, eaav2501 (2019).
- Karunakaran, D. et al. RIPK1 gene variants associate with obesity in humans and can be therapeutically silenced to reduce obesity in mice. *Nat. Metab.* **2**, 1113–1125 (2020).
- Angueira, A. R. et al. Defining the lineage of thermogenic perivascular adipose tissue. *Nat. Metab.* **3**, 469–484 (2021).
- Hao, Y. et al. Integrated analysis of multimodal single-cell data. *Cell* **184**, 3573–3587. e3529 (2021).
- Li, B. et al. Benchmarking spatial and single-cell transcriptomics integration methods for transcript distribution prediction and cell type deconvolution. *Nat. Methods* **19**, 662–670 (2022).
- Dominguez Conde, C. et al. Cross-tissue immune cell analysis reveals tissue-specific features in humans. *Science* **376**, eabl5197 (2022).

19. Eto, H. et al. Characterization of structure and cellular components of aspirated and excised adipose tissue. *Plast. Reconstr. Surg.* **124**, 1087–1097 (2009).
20. Denisenko, E. et al. Systematic assessment of tissue dissociation and storage biases in single-cell and single-nucleus RNA-seq workflows. *Genome Biol.* **21**, 130 (2020).
21. Forcato, M., Romano, O. & Bicciato, S. Computational methods for the integrative analysis of single-cell data. *Brief Bioinform.* **22**, 20–29 (2021).
22. Peng, M., Li, Y., Wamsley, B., Wei, Y. & Roeder, K. Integration and transfer learning of single-cell transcriptomes via cFIT. *Proc. Natl. Acad. Sci. USA* **118**, e2024383118 (2021).
23. Xu, C. et al. Probabilistic harmonization and annotation of single-cell transcriptomics data with deep generative models. *Mol. Syst. Biol.* **17**, e9620 (2021).
24. Polanski, K. et al. BBKNN: fast batch alignment of single cell transcriptomes. *Bioinformatics* **36**, 964–965 (2020).
25. Korsunsky, I. et al. Fast, sensitive and accurate integration of single-cell data with Harmony. *Nat. Methods* **16**, 1289–1296 (2019).
26. Gayoso, A. et al. A Python library for probabilistic analysis of single-cell omics data. *Nat. Biotechnol.* **40**, 163–166 (2022).
27. Luecken, M. D. et al. Benchmarking atlas-level data integration in single-cell genomics. *Nat. Methods* **19**, 41–50 (2022).
28. Tran, H. T. N. et al. A benchmark of batch-effect correction methods for single-cell RNA sequencing data. *Genome Biol.* **21**, 12 (2020).
29. Hubert, L. & Arabie, P. Comparing partitions. *J. Classif.* **2**, 193–218 (1985).
30. Buttner, M., Miao, Z., Wolf, F. A., Teichmann, S. A. & Theis, F. J. A test metric for assessing single-cell RNA-seq batch correction. *Nat. Methods* **16**, 43–49 (2019).
31. Simpson, E. H. Measurement of diversity. *Nature* **163**, 688–688 (1949).
32. Arner, P. et al. The epigenetic signature of systemic insulin resistance in obese women. *Diabetologia* **59**, 2393–2405 (2016).
33. Krieg, L. et al. Multiomics reveal unique signatures of human epiploic adipose tissue related to systemic insulin resistance. *Gut* **71**, 2179–2193 (2021).
34. Chen, L. et al. ITLN1 inhibits tumor neovascularization and myeloid derived suppressor cells accumulation in colorectal carcinoma. *Oncogene* **40**, 5925–5937 (2021).
35. Johnson, M. D. et al. Inhibition of angiogenesis by tissue inhibitor of metalloproteinase. *J. Cell Physiol.* **160**, 194–202 (1994).
36. Medina, R. J. et al. Molecular analysis of endothelial progenitor cell (EPC) subtypes reveals two distinct cell populations with different identities. *BMC Med. Genomics* **3**, 18 (2010).
37. Keighron, C., Lyons, C. J., Creane, M., O'Brien, T. & Liew, A. Recent advances in endothelial progenitor cells toward their use in clinical translation. *Front. Med. (Lausanne)* **5**, 354 (2018).
38. Wang, Q. A., Tao, C., Gupta, R. K. & Scherer, P. E. Tracking adipogenesis during white adipose tissue development, expansion and regeneration. *Nat. Med.* **19**, 1338–1344 (2013).
39. Borrelli, M. R. et al. The antifibrotic adipose-derived stromal cell: grafted fat enriched with CD74+ adipose-derived stromal cells reduces chronic radiation-induced skin fibrosis. *Stem Cells Transl. Med.* **9**, 1401–1413 (2020).
40. Buechler, M. B. et al. Cross-tissue organization of the fibroblast lineage. *Nature* **593**, 575–579 (2021).
41. Ehlund, A. et al. Transcriptional dynamics during human adipogenesis and its link to adipose morphology and distribution. *Diabetes* **66**, 218–230 (2017).
42. Khan, A. et al. SNEV(hPrp19/hPso4) regulates adipogenesis of human adipose stromal cells. *Stem Cell Rep.* **8**, 21–29 (2017).
43. Tini, G. et al. DNA methylation during human adipogenesis and the impact of fructose. *Genes Nutr.* **15**, 21 (2020).
44. Shao, M. et al. Pathologic HIF1alpha signaling drives adipose progenitor dysfunction in obesity. *Cell Stem Cell* **28**, 685–701.e687 (2021).
45. Harms, M. J. et al. Mature human white adipocytes cultured under membranes maintain identity, function, and can transdifferentiate into brown-like adipocytes. *Cell Rep.* **27**, 213–225.e215 (2019).
46. Forrest, A. R. et al. A promoter-level mammalian expression atlas. *Nature* **507**, 462–470 (2014).
47. Gupta, A. et al. Characterization of transcript enrichment and detection bias in single-nucleus RNA-seq for mapping of distinct human adipocyte lineages. *Genome Res.* **32**, 242–257 (2022).
48. Jin, S. et al. Inference and analysis of cell-cell communication using CellChat. *Nat. Commun.* **12**, 1088 (2021).
49. Timokhina, I., Kissel, H., Stella, G. & Besmer, P. Kit signaling through PI 3-kinase and Src kinase pathways: an essential role for Rac1 and JNK activation in mast cell proliferation. *EMBO J.* **17**, 6250–6262 (1998).
50. Huizer, K. et al. Periostin is expressed by pericytes and is crucial for angiogenesis in glioma. *J. Neuropathol. Exp. Neurol.* **79**, 863–872 (2020).
51. Rosen, E. D. & Spiegelman, B. M. What we talk about when we talk about fat. *Cell* **156**, 20–44 (2014).
52. Pasarica, M. et al. Reduced adipose tissue oxygenation in human obesity: evidence for rarefaction, macrophage chemotaxis, and inflammation without an angiogenic response. *Diabetes* **58**, 718–725 (2009).
53. Kerr, A. G., Andersson, D. P., Ryden, M., Arner, P. & Dahlman, I. Long-term changes in adipose tissue gene expression following bariatric surgery. *J. Intern. Med.* **288**, 219–233 (2020).
54. Petrus, P. et al. Transforming growth factor-beta3 regulates adipocyte number in subcutaneous white adipose tissue. *Cell Rep.* **25**, 551–560.e555 (2018).
55. Lenz, M., Arts, I. C. W., Peeters, R. L. M., de Kok, T. M. & Ertaylan, G. Adipose tissue in health and disease through the lens of its building blocks. *Sci. Rep.* **10**, 10433 (2020).
56. Norreen-Thorsen, M. et al. A human adipose tissue cell-type transcriptome atlas. *Cell Rep.* **40**, 111046 (2022).
57. Hoffstedt, J. et al. Long-term protective changes in adipose tissue after gastric bypass. *Diabetes Care* **40**, 77–84 (2017).
58. Mileti, E. et al. Human white adipose tissue displays selective insulin resistance in the obese state. *Diabetes* **70**, 1486–1497 (2021).
59. Ryden, M. et al. The adipose transcriptional response to insulin is determined by obesity, not insulin sensitivity. *Cell Rep.* **16**, 2317–2326 (2016).
60. Slyper, M. et al. A single-cell and single-nucleus RNA-Seq toolbox for fresh and frozen human tumors. *Nat. Med.* **26**, 792–802 (2020).
61. Fleming, S. J., Marioni, J. C. & Babadi, M. CellBender remove-background: a deep generative model for unsupervised removal of background noise from scRNA-seq datasets. *bioRxiv*, <https://www.biorxiv.org/content/10.1101/791699v1> (2019).
62. Germain, P. L., Lun, A., Garcia Meixide, C., Macnair, W. & Robinson, M. D. Doublet identification in single-cell sequencing data using scDblFinder. *F1000Research* **10**, 979 (2022).
63. Team, R. C. R. *A Language and Environment for Statistical Computing*, (Vienna, Austria, 2018).
64. Hafemeister, C. & Satija, R. Normalization and variance stabilization of single-cell RNA-seq data using regularized negative binomial regression. *Genome Biol.* **20**, 296 (2019).
65. Hyvarinen, A. & Oja, E. Independent component analysis: algorithms and applications. *Neural Netw.* **13**, 411–430 (2000).
66. Becht, E. et al. Dimensionality reduction for visualizing single-cell data using UMAP. *Nat. Biotechnol.* **37**, 38–44 (2018).
67. Gustavsen, J. A., Pai, S., Isserlin, R., Demchak, B. & Pico, A. R. RCy3: network biology using cytoscape from within R. *F1000Res* **8**, 1774 (2019).

68. Jew, B. et al. Accurate estimation of cell composition in bulk expression through robust integration of single-cell information. *Nat. Commun* **11**, 1971 (2020).
69. Arner, E. et al. Adipose tissue microRNAs as regulators of CCL2 production in human obesity. *Diabetes* **61**, 1986–1993 (2012).
70. Arner, P., Andersson, D. P., Backdahl, J., Dahlman, I. & Ryden, M. Weight gain and impaired glucose metabolism in women are predicted by inefficient subcutaneous fat cell lipolysis. *Cell Metab.* **28**, 45–54.e43 (2018).
71. Imbert, A. et al. Network analyses reveal negative link between changes in adipose tissue GDF15 and BMI during dietary-induced weight loss. *J. Clin. Endocrinol. Metab.* **107**, e130–e142 (2022).
72. Armenise, C. et al. Transcriptome profiling from adipose tissue during a low-calorie diet reveals predictors of weight and glycemic outcomes in obese, nondiabetic subjects. *Am. J. Clin. Nutr.* **106**, 736–746 (2017).
73. Schwarzer, G., Carpenter, J. R. & Rücker, G. *Meta-Analysis with R* (Springer Cham, 2015).
74. Acosta, J. R. et al. Increased fat cell size: a major phenotype of subcutaneous white adipose tissue in non-obese individuals with type 2 diabetes. *Diabetologia* **59**, 560–570 (2016).
75. Kleshchevnikov, V. et al. Cell2location maps fine-grained cell types in spatial transcriptomics. *Nat. Biotechnol.* **40**, 661–671 (2022).
76. Andersson, A. et al. Single-cell and spatial transcriptomics enables probabilistic inference of cell type topography. *Commun. Biol.* **3**, 565 (2020).
77. Elosua-Bayes, M., Nieto, P., Mereu, E., Gut, I. & Heyn, H. SPOTlight: seeded NMF regression to deconvolute spatial transcriptomics spots with single-cell transcriptomes. *Nucleic Acids Res.* **49**, e50 (2021).
78. Cable, D. M. et al. Robust decomposition of cell type mixtures in spatial transcriptomics. *Nat. Biotechnol.* **40**, 517–526 (2022).
79. Biancalani, T. et al. Deep learning and alignment of spatially resolved single-cell transcriptomes with Tangram. *Nat. Methods* **18**, 1352–1362 (2021).
80. Lopez, R. et al. DestVI identifies continuums of cell types in spatial transcriptomics data. *Nat. Biotechnol.* **40**, 1360–1369 (2022).
81. Noguchi, S. et al. FANTOM5 CAGE profiles of human and mouse samples. *Sci. Data* **4**, 170112 (2017).

Acknowledgements

We thank the National Genomics Infrastructure (NGI) in Genomics Production Stockholm, the Swedish National Infrastructure for Computing (SNIC) at UPPMAX, and the Centre for Bioinformatics and Biostatistics at the Karolinska Institutet for providing support regarding sequencing and computational infrastructure. We also thank Drs. Ana Maria Suzuki and Thais de Castro Barbosa for valuable technical help in processing the clinical samples. Fluorescent imaging was performed at the Live Cell imaging Core facility/Nikon Center of Excellence, at the Karolinska Institute, supported by grants from the Swedish Research Council, KI infrastructure, and Centre for Innovative Medicine. This work was supported by grants from Margareta af Uggle's foundation (M.R.), Knut & Alice Wallenberg's foundation (M.R.), the Swedish Research Council (M.R., P.L.S., N.M.), ERC-SyG SPHERES (856404 to M.R. & D.L.), the European Communities (DiOGenes, FP6-513946, from the European Commission Food Quality and Safety Priority of the Sixth Framework Program [Coordinator W Saris, RTD1 leader Arne Astrup]), the Novo-Nordisk Foundation (including the Tripartite Immuno-metabolism Consortium Grant Number NNF15CC0018486, the MSAM consortium NNF15SA0018346 and the MeRIAD consortium Grant number 0064142, all three M.R. and NNF20OC0061149 to N.M.), CIMED (N.M. and M.R.), the Swedish Diabetes Foundation (M.R.), the Stockholm County Council (M.R.), the Strategic Research Program in Diabetes at Karolinska Institutet (M.R. and N.M.), and the European Foundation for

the Study of Diabetes/Novo Nordisk Foundation Future Leaders Award (N.M.). J.J. and M.E. are supported by PhD-student grants (KID) from Karolinska Institute. L.M. is supported by a postdoctoral grant from the Swedish Society for Medical Research (SSMF). S.F.C. is supported by a Novo Nordisk postdoctoral fellowship run in partnership with Karolinska Institutet. M.L. is supported by grants from the Swedish Childhood Cancer Fund.

Author contributions

L.M., M.R., and N.M. conceived the study and wrote the first draft of the manuscript. L.M., J.J., M.E., J.Z., T.W., P.A.N.N., J.B., C.W., and M.B.L. generated and/or analyzed the single-cell data. J.J., M.E., S.F.C., N.S., T.S., J.L., M.Bu., and M.L. performed, analyzed, or supervised flow-cytometry and immunofluorescence experiments. L.M., J.Z., N.B., A.An., and P.L.S. generated and analyzed the spatial transcriptomics data. A.V., A.As., E.E.B., N.V., and D.L. generated bulk transcriptomic data from the DioGenes cohort and A.G.K. from the DEOSH cohort, results which were further processed by L.M. and N.V. Cluster annotations were performed by L.M., J.J., M.E., J.B., N.S., B.T.P.T., M.Bu., M.L., and K.K. Critical intellectual input to shape the study design was provided by D.L., C.W., and M.B.L. All authors read and approved the final version of the manuscript.

Funding

Open access funding provided by Karolinska Institute.

Competing interests

P.L.S. and N.B. are scientific consultants to 10x Genomics, which holds IP rights to the spatial transcriptomics technology. None of the other authors have any conflict of interest to report.

Additional information

Supplementary information The online version contains supplementary material available at <https://doi.org/10.1038/s41467-023-36983-2>.

Correspondence and requests for materials should be addressed to Mikael Rydén or Niklas Mejhert.

Peer review information : *Nature Communications* thanks the anonymous reviewers for their contribution to the peer review of this work. Peer reviewer reports are available.

Reprints and permissions information is available at <http://www.nature.com/reprints>

Publisher's note Springer Nature remains neutral with regard to jurisdictional claims in published maps and institutional affiliations.

Open Access This article is licensed under a Creative Commons Attribution 4.0 International License, which permits use, sharing, adaptation, distribution and reproduction in any medium or format, as long as you give appropriate credit to the original author(s) and the source, provide a link to the Creative Commons license, and indicate if changes were made. The images or other third party material in this article are included in the article's Creative Commons license, unless indicated otherwise in a credit line to the material. If material is not included in the article's Creative Commons license and your intended use is not permitted by statutory regulation or exceeds the permitted use, you will need to obtain permission directly from the copyright holder. To view a copy of this license, visit <http://creativecommons.org/licenses/by/4.0/>.

© The Author(s) 2023

¹Department of Medicine Huddinge (H7), Karolinska Institutet, Karolinska University Hospital Huddinge, SE-141 83, Huddinge, Sweden. ²Laboratory of Translational Nutrition Biology, Institute of Food, Nutrition and Health, Department of Health Sciences and Technology, ETH Zurich, Schwerzenbach, Switzerland. ³Helmholtz Institute for Metabolic, Obesity and Vascular Research (HI-MAG) of the Helmholtz Zentrum München at the University of Leipzig and University Hospital Leipzig, Leipzig, Germany. ⁴Center for Infectious Medicine, Department of Medicine Huddinge (H7), Karolinska Institutet, Karolinska University Hospital Huddinge, SE-141 52, Huddinge, Sweden. ⁵Childhood Cancer Research Unit, Department of Women's and Children's Health, Karolinska Institutet, SE-171 77, Stockholm, Sweden. ⁶Department of Clinical Science, Intervention & Technology (CLINTEC), Unit of Renal Medicine, Karolinska Institutet, Karolinska University Hospital Huddinge, SE-141 86, Huddinge, Sweden. ⁷Science for Life Laboratory, Department of Gene Technology, KTH Royal Institute of Technology, SE-171 65, Solna, Sweden. ⁸Department of Metabolic Health, Nestle Institute of Health Sciences, Nestle Research, Lausanne, Switzerland. ⁹Department of Obesity and Nutritional Sciences, The Novo Nordisk Foundation, Hellerup, Denmark. ¹⁰Department of Human Biology, NUTRIM School of Nutrition and Translational Research in Metabolism, Maastricht University Medical Centre(+), Maastricht, the Netherlands. ¹¹Institute of Metabolic and Cardiovascular Diseases (I2MC), Institut National de la Santé et de la Recherche Médicale (Inserm), Université Toulouse III - Paul Sabatier (UPS), Université de Toulouse, UMR1297 Toulouse, France. ¹²Franco-Czech Laboratory for Clinical Research on Obesity, Third Faculty of Medicine, Charles University, Prague and Université Toulouse III - Paul Sabatier (UPS), Toulouse, France. ¹³Laboratoire de biochimie, Centre Hospitalier Universitaire de Toulouse, Toulouse, France. ¹⁴Institut Universitaire de France (IUF), Paris, France. ¹⁵Medical Department III - Endocrinology, Nephrology, Rheumatology, University of Leipzig Medical Center, Leipzig, Germany. ¹⁶These authors contributed equally: Mikael Rydén, Niklas Mejhert.

✉ e-mail: mikael.ryden@ki.se; niklas.mejhert@ki.se